

# A consistent solution of the re-initialization equation in the conservative level-set method

Tomasz Waclawczyk\*

*Institute of Numerical Methods in Mechanical Engineering,  
Technische Universität Darmstadt,  
Dolivostr. 15, 64293 Darmstadt, Germany*

---

## Abstract

In this paper, a new re-initialization method for the conservative level-set function is put forward. First, it has been shown that the re-initialization and advection equations of the conservative level-set function are mathematically equivalent to the re-initialization and advection equations of the localized signed distance function. Next, a new discretization for the spatial derivatives of the conservative level-set function has been proposed. This new discretization is consistent with the re-initialization procedure and it guarantees a second-order convergence rate of the interface curvature on gradually refined grids. The new re-initialization method does not introduce artificial deformations to stationary and non-stationary interfaces, even when the number of re-initialization steps is large.

*Keywords:* conservative level-set method, consistent re-initialization, localized signed distance function, interface capture, multiphase flows

*2010 MSC:* 00-01, 99-00

---

## 1. Introduction

In the conservative level-set method introduced by Olsson and Kreiss [1], a solution of the transport equation of the characteristic function  $\alpha(\mathbf{x}, t)$  is

---

\*Tomasz Waclawczyk  
*Email address:* `twacl@fmb.tu-darmstadt.de` (Tomasz Waclawczyk)

divided into two steps: advection and re-initialization. These two steps are carried out consecutively in only one single time step  $\Delta t$ . The solution of the  $\alpha(\mathbf{x}, t)$  advection equation is typically performed using an explicit or implicit time discretization with a TVD MUSCL flux limiter, in order to keep  $0 \leq \alpha(\mathbf{x}, t) \leq 1$  a bounded function [1, 2, 3, 4, 5]. The present work provides improvements in the second step of the above interface capturing procedure. Let us consider the re-initialization equation

$$\frac{\partial \alpha}{\partial \tau} = \nabla \cdot [D|\nabla \alpha| \mathbf{n}_\Gamma - C\alpha(1 - \alpha) \mathbf{n}_\Gamma], \quad (1)$$

where  $\alpha(\mathbf{x}, t)$  denotes a regularized Heaviside function,  $\tau$  is the artificial time,  $\mathbf{n}_\Gamma = \nabla \alpha / |\nabla \alpha|$  is a vector normal to the iso-lines (iso-surfaces) of  $\alpha(\mathbf{x}, t)$ . We assume that  $C = 1 \text{ m/s}$ ,  $D = \Delta x / 2C = \epsilon_h C$  where  $\Delta x = \Delta y = \Delta z = 1/N_c$  is the size a control volume and  $N_c$  is the total number of control volumes in the  $x$ ,  $y$  or  $z$  direction.

In [1] it has been shown the solution of Eq. (1) after advection of  $\alpha(\mathbf{x}, t)$ , reduces artificial deformations of the interface induced by numerical errors during the advection step. Therein it was also noticed that the analytical solution to the stationary equation (1) is given by

$$\alpha(\psi_0(\mathbf{x}, t)) = 1 - \frac{1}{1 + \exp(\psi_0(\mathbf{x}, t) / \epsilon_h)} = \frac{1}{2} \left[ 1 + \tanh \left( \frac{\psi_0(\mathbf{x}, t)}{2\epsilon_h} \right) \right], \quad (2)$$

where  $\psi_0(\mathbf{x}, t)$  is the signed distance function [5, 6, 7]. When  $\epsilon_h \rightarrow 0$ , then  $\alpha(\psi_0)$  in equation (2) tends to the phase indicator function which is given by the exact Heaviside function  $H(\psi_0)$  as is demonstrated in Appendix A. The phase indicator function  $H(\psi_0)$  is typically discretized in the volume of fluid (VOF) family of methods satisfying the law of conservation of mass [8]. In real simulations  $\epsilon_h \neq 0$ , and hence  $\alpha(\psi_0)$  in equation (2) is not represented by a sharp jump localized at the interface  $\Gamma$ . The level-set function  $\alpha(\psi_0)$  is a Lipschitz continuous function and, therefore, resembles the signed distance function in the standard level-set (LS) method introduced by Osher and Sethian [9] and extended by Sussman et al. [10, 11]. For these reasons, Olsson and Kreiss [1] called their interface capturing technique the conservative level-set

(CLS) method. The signed distance function derived from Eq. (2) is given by the equation

$$\psi_0(\alpha) = \epsilon_h \ln \left[ \frac{\alpha(\psi_0)}{1 - \alpha(\psi_0)} \right]. \quad (3)$$

We note that in Eq. (2) the interface  $\Gamma$  is localized at  $\alpha(\mathbf{x}_\Gamma, t) = 1/2$  whereas in Eq. (3) the set of points where the signed distance function  $\psi_0(\alpha(\mathbf{x}_\Gamma, t) = 1/2) = 0$  represents a position of the interface  $\Gamma$ .

A mapping between  $\alpha(\psi_0)$  and  $\psi_0(\alpha)$  in equations (2) and (3) suggests a closer relation between the CLS method and the standard LS method exists. In the present paper, we show how this relation can be established. Moreover, we put forward a new method for computation of higher-order spatial derivatives of  $\alpha(\psi_0)$ , which is consistent with the new re-initialization procedure. The spatial derivatives of  $\alpha(\psi_0)$  obtained with our new method are later used to approximate the interface curvature  $\kappa$  with second-order accuracy.

A relation between the regularized Heaviside function and the signed distance function was first observed by Glasner [6], and was used for a non-linear preconditioning of the phase-field equation. The non-linear preconditioning was later exploited by Sun and Beckermann [7] in order to solve the phase-field equation in a context of the interface capturing. Therein, it was mentioned that the stationary solutions to the phase-field equation and to equation (1) are different. Later in this paper, the key differences between the present results and the results reported in [7] are addressed.

The main difficulty in using  $\alpha(\psi_0)$  and  $\psi_0(\alpha)$  interchangeably is the lack of a correct numerical solution to the re-initialization equation (1). Although vast literature concerning the numerical solution of the re-initialization equation for the signed distance function exists, see [12, 13, 14] to name only a few recent works, the solution of equation (1) has drawn less attention. In [1] the re-initialization equation (1) is solved directly, in [15] to reduce artificial interface deformations due to discretization errors; the diffusive term in Eq. (1) was projected on  $\mathbf{n}_\Gamma$ , however as it is shown by Shukla et al. [2], this reformulation leads to numerical instabilities. Recently, McCaslin and Desjardins [16] pro-

posed to multiply diffusive and compressive fluxes on the right-hand side (RHS) of Eq. (1) by a new function  $\beta(\mathbf{x}, t)$ . This allows them to vary the number of steps in their re-initialization procedure depending on the local flow conditions, thus reducing artificial deformations of the interface.

Shukla et al. in [2] assume that Eq. (1) has no physical meaning, and thus it can be solved in the non-conservative form without the term containing the interface curvature  $\kappa = -\nabla \cdot \mathbf{n}_\Gamma$ . With such an assumption, the counteracting diffusive and compressive fluxes in Eq. (1) are projected only on the direction normal to the interface  $\mathbf{n}_\Gamma$

$$\frac{\partial \alpha}{\partial \tau} = \mathbf{n}_\Gamma \cdot \nabla [\epsilon_h |\nabla \alpha| - \alpha(1 - \alpha)]. \quad (4)$$

Moreover, in [2] it has been shown the key element which guarantees the successful numerical solution of Eq. (4) is the discretization of  $|\nabla \alpha| = |\nabla \psi| F(\alpha, \gamma)$ , where  $\psi$  is a mapping function which smooths  $\alpha(\mathbf{x}, t)$  and allows to compute  $|\nabla \alpha|$  with a smaller error.

Since in [1, 2, 4, 5, 15, 16] the discretization and solution of Eq. (1) are only briefly addressed, in this paper we mainly focus on the discretization and solution of Eq. (1) in the framework of the second-order accurate finite volume method. In particular, we are interested in the case where the number of re-initialization steps in the numerical solution of Eq. (1) is  $N_\tau \gg 1$  and the interface  $\Gamma$  is stationary. As it is described by McCaslin and Desjardins [16], in such circumstances  $\Gamma$  is especially prone to artificial deformations caused by errors in calculations of  $\alpha(\psi_0)$  and  $\mathbf{n}_\Gamma$ .

The outline of this paper is as follows. In Section 2, the influence of the mapping function  $\psi(\alpha, \gamma)$  introduced in [2] on a convergence rate of numerical solutions to Eq. (1) is analyzed. In Section 3, we show that under certain conditions the mapping function  $\psi(\alpha, \gamma)$  approximates the signed distance function  $\psi_0(\alpha)$  up to higher-order terms. For this reason, in the present work, it is proposed to use the signed distance function  $\psi_0(\alpha)$  as the new mapping function in the discretization of  $|\nabla \alpha|$  in Eq. (1). Consequently, Section 4 presents the selection of the mapping function  $\psi$  further leads to a new, mathematically

consistent method for computation of spatial derivatives of  $\alpha(\psi_0)$ , and thus, the interface curvature. This allows us to reformulate the re-initialization and advection equations of the conservative level-set function  $\alpha(\psi_0)$  in Section 5. Moreover, in Section 5, we show mathematical equivalence between the CLS method where the interface  $\Gamma$  is represented by  $\alpha(\psi_0)$  and the standard LS method where the interface is represented by  $\psi_0(\alpha)$ , localized at the interface by Dirac's delta. In Section 6, we investigate properties of the newly formulated re-initialization and advection equations, in particular their convergence rates and errors in approximation of spatial derivatives of  $\alpha(\psi_0)$  used to compute the interface curvature. Finally, the new re-initialization method is examined in several test cases with advection in order to closely inspect its conservative properties.

## 2. Selection of the mapping function

To assure convergence of equation (4) during integration in time  $\tau$ , in [2] the mapping function  $\psi(\alpha, \gamma)$  that smooths  $\alpha(\mathbf{x}, t)$  was introduced for discretization of  $|\nabla\alpha|$ . Therein it was also noticed that  $\psi(\alpha, \gamma)$  has to satisfy two conditions, the first condition is given by the equality

$$\frac{\nabla\alpha}{|\nabla\alpha|} = \frac{\nabla\psi}{|\nabla\psi|}, \quad (5)$$

as the mapping cannot change directions of the vectors normal to  $\alpha(\mathbf{x}, t)$  iso-surfaces. The second condition demands that the linear relation between  $\nabla\psi$  and  $\nabla\alpha$  exists

$$\nabla\alpha = F(\alpha, \gamma) \nabla\psi, \quad (6)$$

where  $F(\alpha, \gamma)$  is a known function and  $0 < \gamma < 1$  is a constant. In this work, we show that the condition given by Eq. (6) can be also used to compute the second-order spatial derivatives of the conservative level-set function  $\alpha(\psi(\mathbf{x}, t))$

$$\alpha_{,ij} = F(\alpha, \gamma) \left[ \psi_{,ij} + \psi_{,i} \psi_{,j} \frac{\partial F}{\partial \alpha} \right], \quad (7)$$

when the mapping function  $\psi$  has been chosen properly,  $\alpha_{,ij} = \partial^2\alpha/\partial x_i\partial x_j$  and  $i, j = 1, 2, 3$ . Equation (7) is required for a consistent approximation of the interface curvature  $\kappa$ .

Unlike in works [2, 4], in this paper we use the mapping functions  $\psi$  for discretization of  $|\nabla\alpha|$  in equation (1). First, we note that the definition of the mapping function  $\psi_1(\alpha, \gamma)$  from [2]

$$\psi_1(\alpha, \gamma) = \frac{(\alpha + \epsilon)^\gamma}{(\alpha + \epsilon)^\gamma + (1 - \alpha + \epsilon)^\gamma}, \quad (8)$$

where originally  $\epsilon = 0$ , introduces discontinuities in the initial condition to Eq. (1) as it is depicted in Fig. 1(a). Two discontinuities are caused by the arithmetic underflow when  $\alpha \rightarrow 0$  and  $1 - \alpha \rightarrow 0$ . In order to avoid this, a straightforward modification of the mapping function from [2] is introduced. In figure 1(a) we show that setting  $\epsilon = 5 \cdot 10^{-16}$  allows avoiding jumps in  $\psi_1$ . Since the arithmetic or floating point underflow is a purely numerical phenomenon, we always set  $\epsilon = 0$  when analytical operations using Eq. (8) are performed.

This minor modification in Eq. (8)) has a great impact on convergence of the numerical solution to Eq. (1). In figure 1(b) convergence of the solutions to Eq. (1) in the case of re-initialization of the 1D regularized Heaviside function is presented, in this figure the distance between solutions on two different time levels is measured by the first-order norm

$$L_1 = \frac{1}{N_c} \sum_{l=1}^{N_c} |\alpha_l^{n+1} - \alpha_l^n|, \quad (9)$$

where  $N_c$  is the number of control volumes and  $n + 1$  denotes a new time level. In this study, the initial condition to Eq. (1) is given by Eq. (2) and we use three different functions in the second-order central differencing discretization of  $|\nabla\alpha|$ :  $\alpha$  alone without smoothing, the original mapping function from [2] where  $\epsilon = 0$ , and the modified mapping function given by Eq. (8) where  $\epsilon \neq 0$ . As in [2, 4] we use the value  $\gamma = 0.1$  in Eq. (8). Re-initialization of the 1D regularized Heaviside function is performed in the computational domain  $\Omega = \langle 0, 1 \rangle_m$  where the interface  $\Gamma$  is located at  $x_\Gamma = 0.5m$ ; the mesh distribution is uniform  $\Delta x = 1/N_c$ ,  $N_c = 128$  is the number of control volumes. At all boundaries of

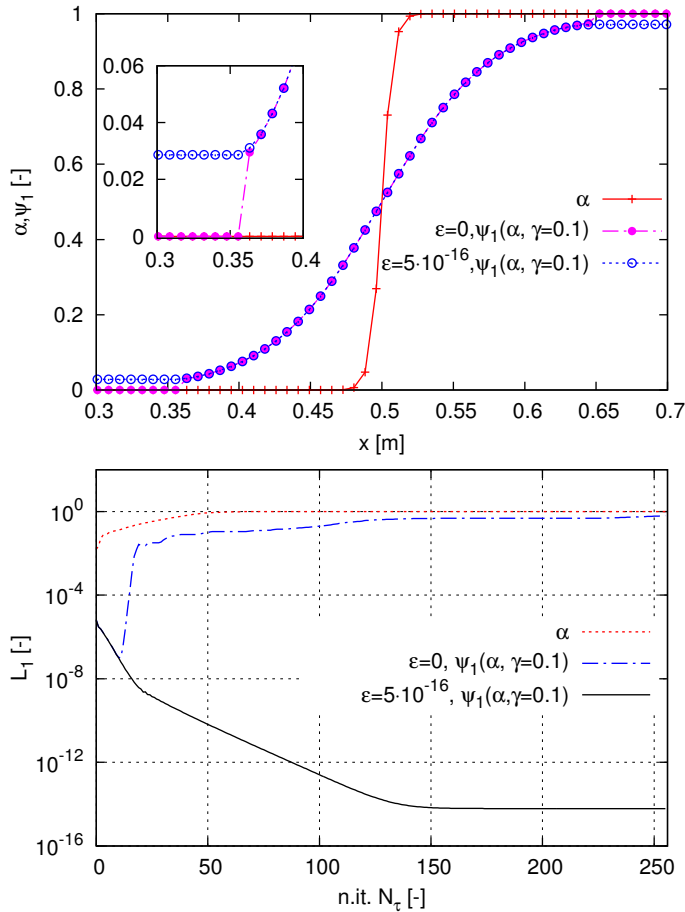


Figure 1: Re-initialization of the 1D regularized Heaviside function  $H(x - 0.5)$ : (a) influence of  $\epsilon \neq 0$  in Eq. (8) on the presence of discontinuities appearing due to arithmetical underflow, (b) convergence of the solution to Eq. (1) with different discretizations of  $|\nabla\alpha|$ :  $\alpha$  without smoothing,  $\psi_1(\alpha, \gamma)$  where  $\epsilon = 0$  and  $\psi_1(\alpha, \gamma)$  where  $\epsilon = 5 \cdot 10^{-16}$ ,  $\gamma = 0.1$  in all cases.  $L_1$  norm is defined by Eq. (9).

the computational domain  $\Omega$ , the Neumann boundary condition for  $\alpha(\psi_0)$  is used. In our second-order accurate finite volume solver Fastest, the third order TVD Runge-Kutta method introduced in [17] is used to integrate Eq. (1) in the time  $\tau$ ; the time step size is set to  $\Delta\tau = D/C^2 = \epsilon_h$ . More details concerning discretization of Eq. (1) in the Fastest flow solver can be found in Appendix B.

Since the initial condition to Eq. (1) is given by Eq. (2), we expect an

immediate convergence of its solution to numerical zero because equation (1) is initialized with its own analytical solution. However, in Fig. 1(b) it is observed that only the solution with  $\epsilon \neq 0$  in Eq. (8) allows convergence during all  $N_\tau = 256$  time steps.

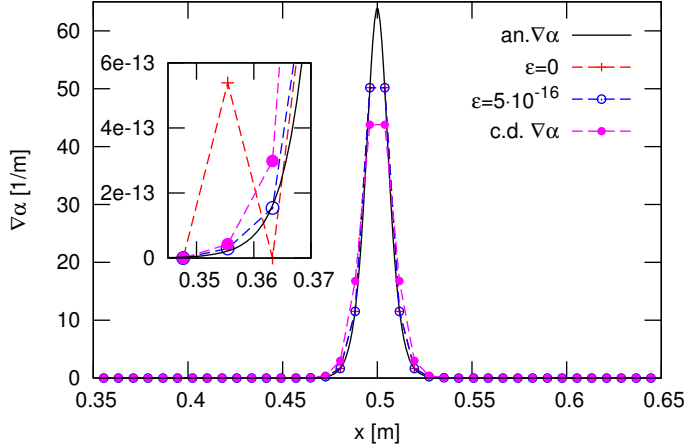


Figure 2: The comparison of  $|\nabla\alpha|$  after  $N_\tau = 1$  re-initialization steps of the 1D regularized Heaviside function with the central difference gradient approximation (c.d.  $\nabla\alpha$ ) and analytical gradient (black solid line). The  $|\nabla\alpha|$  in equation (1) is discretized using the mapping function  $\psi_1(\alpha, \gamma)$  with  $\epsilon = 0$  and  $\epsilon = 5 \cdot 10^{-16}$ ,  $\gamma = 0.1$ .

To explain differences in the convergence rates which are observed in Fig. 1(b), in figures 2 and 3 we compare the first-order derivatives of  $\alpha(\psi_0)$  and  $L_1(\nabla\alpha)$  norms after  $N_\tau = 1$  re-initialization steps. In figure 3, the  $L_1(\nabla\alpha)$  norm is defined by the equation

$$L_1(\phi) = \frac{|\phi_{an} - \phi_{num}|}{|\phi_{an}| + \epsilon}, \quad (10)$$

where  $\phi_{an}$ ,  $\phi_{num}$  are functions calculated, respectively, analytically and numerically in each control volume,  $\epsilon = 5 \cdot 10^{-16}$  and  $\phi = \nabla\alpha$ .

In figures 2 and 3, it is observed that both original  $\epsilon = 0$  and modified  $\epsilon = 5 \cdot 10^{-16}$  mapping functions provide very good approximations of  $|\nabla\alpha|$  when compared with central difference gradient approximation. Differences between these two gradient approximations are visible only around  $x = 0.35 m$  and

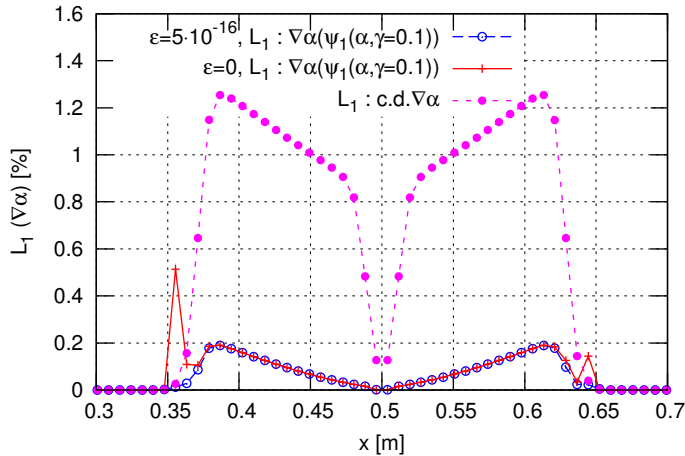


Figure 3: Distributions of  $L_1(\nabla\alpha)$  norm defined by Eq. (10) after  $N_\tau = 1$  re-initialization steps during re-initialization of the 1D regularized Heaviside function. The error  $L_1$  is calculated for three  $|\nabla\alpha|$  approximations depicted in Fig. 1.

$x = 0.65 m$  where the jumps in  $\psi_1$  are present (compare results presented in figure 1 and in figures 2-3). If the mapping function is defined by Eq. (8) with  $\epsilon = 5 \cdot 10^{-16}$ , the artificial oscillations are absent since  $\psi_1$  is continuous everywhere. The continuity of  $\psi_1$  guarantees convergence of the solution to equation (1) during all re-initialization steps as shown in Fig. 1(b). From now on, when referring to the mapping function  $\psi_1$ , we reference its definition given by Eq. (8) with  $\epsilon = 5 \cdot 10^{-16}$ .

### 3. Relation between the mapping function and the signed distance function

Figure 1(b) shows the minor modification of the mapping function  $\psi_1$  guarantees convergence of the numerical solution to Eq. (1) during all re-initialization steps. Here, we also note that this discretization requires about  $N_\tau \approx 140$  time steps  $\Delta\tau$  to achieve the stationary solution in spite of the fact that Eq. (1) is initialized with its stationary solution given by Eq. (2). Therefore, the mapping function  $\psi_1(\alpha, \gamma = 0.1)$  where  $\epsilon = 5 \cdot 10^{-16}$  is not the best possible choice for discretization of  $|\nabla\alpha|$  in Eq. (1). Hence, there is a need for an improved

discretization of  $|\nabla\alpha|$ , guaranteeing immediate convergence of the numerical solution to Eq. (1) towards a steady state.

In this section, we have shown when  $0 < N_c\gamma \ll 1$  or equivalently  $0 < \gamma \ll \Delta x$ , the mapping function  $\psi_1(\alpha, \gamma)$  given by Eq. (8) approximates the signed distance function  $\psi_0(\alpha)$  up to higher-order terms. Let us first note that the stationary solution (2) can be rewritten as

$$\alpha(\psi_0) = \frac{1}{2} \left[ 1 + \tanh\left(\frac{\psi_0}{2\epsilon_h}\right) \right] = \frac{\exp(N_c\psi_0)}{\exp(N_c\psi_0) + \exp(-N_c\psi_0)}. \quad (11)$$

Next, we observe that

$$\alpha^\gamma = \frac{\exp(N_c\gamma\psi_0)}{[\exp(N_c\psi_0) + \exp(-N_c\psi_0)]^\gamma}, \quad (12)$$

$$(1 - \alpha)^\gamma = \frac{\exp(-N_c\gamma\psi_0)}{[\exp(N_c\psi_0) + \exp(-N_c\psi_0)]^\gamma}, \quad (13)$$

and we substitute Eqs. (12) and (13) into Eq. (8) to obtain

$$\psi_1 = \frac{\exp(N_c\psi_0\gamma)}{\exp(N_c\psi_0\gamma) + \exp(-N_c\psi_0\gamma)}. \quad (14)$$

Now, we expand exponents in Eq. (14) in the Taylor series

$$\exp(N_c\psi_0\gamma) = 1 + N_c\psi_0\gamma + \frac{(N_c\psi_0\gamma)^2}{2!} + \frac{(N_c\psi_0\gamma)^3}{3!} + \dots \quad (15)$$

$$\exp(-N_c\psi_0\gamma) = 1 - N_c\psi_0\gamma + \frac{(N_c\psi_0\gamma)^2}{2!} - \frac{(N_c\psi_0\gamma)^3}{3!} + \dots \quad (16)$$

If  $0 < N_c\gamma \ll 1$  is sufficiently small then the higher-order terms in Eqs. (15) and (16) can be neglected what gives

$$\exp(N_c\psi_0\gamma) = 1 + N_c\psi'_0\gamma, \quad (17)$$

$$\exp(-N_c\psi_0\gamma) = 1 - N_c\psi'_0\gamma, \quad (18)$$

where  $\psi'_0 \approx \psi_0$ . After substitution of Eqs. (17) and (18) into Eq. (14) one obtains

$$\psi_1 = \frac{1 + N_c\psi'_0\gamma}{2} = \frac{1}{2} \left( 1 + \frac{\gamma}{2\epsilon_h} \psi'_0 \right). \quad (19)$$

Eq. (19) is the exact relation between  $\psi_1$  and  $\psi'_0$  when  $0 < N_c\gamma \ll 1$ . Next, from Eq. (19) we derive the relation between the signed distance function  $\psi_0$  its

approximation  $\psi'_0$  and the mapping function  $\psi_1(\alpha, \gamma)$

$$\psi_0 \approx \psi'_0 = \frac{2\epsilon_h}{\gamma} (2\psi_1 - 1). \quad (20)$$

We note that the absolute value of the gradient of  $\psi_0 \approx \psi'_0$

$$\left| \frac{\partial \psi_0}{\partial x_i} \right| \approx \left| \frac{\partial \psi'_0}{\partial x_i} \right| = \left| \frac{\partial \psi'_0}{\partial \psi_1} \frac{\partial \psi_1}{\partial x_i} \right| = \left| \frac{4\epsilon_h}{\gamma} \frac{\partial \psi_1}{\partial x_i} \right| = 1 \quad (21)$$

since  $|\nabla \psi_0| = 1$  is the property of the signed-distance function, see [9, 12]. In 1D the second-order derivative of  $\psi_0 \approx \psi'_0$  is equal to zero

$$\frac{\partial}{\partial x_1} \left( \frac{\partial \psi_0}{\partial x_1} \right) \approx \frac{\partial}{\partial x_1} \left( \frac{\partial \psi'_0}{\partial x_1} \right) = \frac{\partial}{\partial x_1} \left( \frac{4\epsilon_h}{\gamma} \frac{\partial \psi_1}{\partial x_1} \right) = 0. \quad (22)$$

The remaining question to be considered is how to select a value of the constant  $\gamma$  in the above equations; the answer to this problem is given in Section 5.1. Next, we show how to use the mapping functions  $\psi_0 \approx \psi'_0$  to compute spatial derivatives of  $\alpha(\psi_0)$  and  $\alpha(\psi'_0)$ , as this leads to reformulation of equation (1).

#### 4. Computation of spatial derivatives with mapping functions

In this section we derive formulas for the first and second-order spatial derivatives of the conservative level-set function  $\alpha(\mathbf{x}, t)$ , see Eqs. (6) and (7). These new formulations exploit dependence of the level-set function  $\alpha$  on the signed distance function  $\psi_0(\alpha)$  or its approximation  $\psi'_0(\psi_1)$ , see Eq. (3) or Eq. (20), respectively.

Let us first calculate  $\alpha_{,i} = \partial \alpha / \partial x_i$ ,  $i = 1, 2, 3$  using Eq. (8), in this case the first-order spatial derivative is given by the equation

$$\alpha_{,i} = \frac{\zeta^2 \delta^{1-\gamma}}{\gamma} \psi_{1,i} = F(\alpha, \gamma) \psi_{1,i}, \quad (23)$$

where  $\zeta(\alpha, \gamma)$  and  $\delta(\alpha)$  are two auxiliary functions

$$\zeta(\alpha, \gamma) = \alpha^\gamma + (1 - \alpha)^\gamma, \quad (24)$$

$$\delta(\alpha) = \alpha(1 - \alpha). \quad (25)$$

The second-order spatial derivatives of  $\alpha(\psi'_0(\psi_1))$  are obtained directly from Eq. (23) and they read

$$\alpha_{,ij} = \frac{\delta^{1-\gamma}\zeta^2}{\gamma} \left\{ \psi_{1,ij} + \frac{\zeta}{\gamma}\psi_{1,i}\psi_{1,j} \right. \\ \left. \left[ 2\gamma \left( (1-\alpha)^{1-\gamma} - \alpha^{1-\gamma} \right) + (1-\gamma)(1-2\alpha)\zeta\delta^{-\gamma} \right] \right\}, \quad (26)$$

where  $\alpha_{,ij} = \partial^2\alpha/\partial x_i\partial x_j$   $i, j = 1, 2, 3$ .

Next, derivatives of  $\alpha(\psi_0(\mathbf{x}, t))$  in terms of the signed distance function  $\psi_0(\alpha)$  are calculated, see Eq. (3), which leads to

$$\alpha_{,i} = \frac{\delta(\alpha)}{\epsilon_h}\psi_{0,i} \quad (27)$$

where  $i = 1, 2, 3$  and  $\delta(\alpha)$  is defined by Eq. (25). The second-order derivative of  $\alpha(\psi_0(\mathbf{x}, t))$  is calculated directly from Eq. (27) as

$$\alpha_{,ij} = \frac{\delta(\alpha)}{\epsilon_h} \left[ \psi_{0,ij} + \frac{1}{\epsilon_h}\psi_{0,i}\psi_{0,j}(1-2\alpha) \right], \quad (28)$$

where  $i, j = 1, 2, 3$ .

We observe that interesting similarities between Eq. (23) and Eq. (27) or Eq. (26) and Eq. (28) do exist when  $0 < \gamma \ll \Delta x$ . For instance, in the case of both mapping functions, the right-hand sides of derived formulations are multiplied by  $\delta(\alpha)/\epsilon_h$ , and it is possible to show that

$$\frac{1}{\epsilon_h} \int_{-\infty}^{\infty} \delta(\alpha) d\psi_0 = 1. \quad (29)$$

Hence,  $\delta(\alpha)/\epsilon_h$  approximates Dirac's delta localized at the interface  $\Gamma$  as it has a compact support (on the given grid as shown in figures 2 and 3) and for  $\epsilon_h \neq 0$  it is  $C^\infty$ . Consequently,  $\delta(\alpha)/\epsilon_h$  restricts the support of  $\alpha_{,i}$ ,  $\alpha_{,ij}$  derivatives to the region localized in the vicinity of the interface  $\Gamma$ .

Next, we note that for  $0 < \gamma \ll \Delta x$  (see condition required to derive Eq. (20))  $\zeta(\alpha, \gamma) \approx 2$  inside the support of  $\delta(\alpha)/\epsilon_h$ , see Eq. (24). With this latter observation and from a comparison between Eq. (23) and Eq. (27) the relation between  $\gamma$  and  $\epsilon_h$  is obtained

$$\frac{\gamma}{4} \approx \epsilon_h. \quad (30)$$

Eq. (30) provides the condition of equality between the first and the second order spatial derivatives of  $\alpha(\psi_0)$  computed using the mapping function  $\psi_1(\alpha, \gamma)$  or  $\psi_0(\alpha)$ , see also Eqs. (21) and (22).

Finally, we recognize the relation between the present results and the result from the theory of distributions, see [18] page 788. When  $\epsilon_h \rightarrow 0$  then  $\alpha(\psi_0) \rightarrow H(\psi_0)$  and  $\delta(\alpha)/\epsilon_h \rightarrow \delta(\psi_0)$ , in such case equation (23) (for  $0 < \gamma \ll \Delta x$ ) and equation (27) read

$$\nabla H(\psi_0) = \delta(\psi_0) \nabla \psi_0, \quad (31)$$

where  $H(\psi_0)$  is the exact Heaviside function and  $\delta(\psi_0)$  is the exact Dirac delta function, both functions are localized at the interface  $\Gamma(\psi_0 \approx \psi'_0 = 0)$ . In particular, in the direction normal to the interface  $\mathbf{n}_\Gamma$ , this definition holds only when  $|\nabla \psi_0| \approx |\nabla \psi'_0| = 1$ . For this reason,  $\psi_0 \approx \psi'_0$  has to be the signed distance function to satisfy the relation between  $\nabla H(\psi_0)$  and  $\delta(\psi_0)$  in equation (31).

## 5. Reformulation of the re-initialization equation

After substitution of Eq. (27) into Eq. (1) the new form of the re-initialization equation is obtained

$$\frac{\partial \alpha}{\partial \tau} = \nabla \cdot [\delta(\alpha) (|\nabla \psi_0| - 1) \mathbf{n}_\Gamma], \quad (32)$$

where  $\delta(\alpha)$  is defined by Eq. (25) and  $\mathbf{n}_\Gamma = \nabla \psi_0 / |\nabla \psi_0|$ , see Eq. (5). We note that  $\partial \alpha / \partial \tau \equiv 0$  when  $|\nabla \psi_0| = 1$  or when  $\delta(H) = 0$ . In the non-conservative form, equation (32) reads

$$\begin{aligned} \frac{\partial \alpha}{\partial \tau} &= \mathbf{n}_\Gamma \cdot \nabla \delta(\alpha) (|\nabla \psi_0| - 1) \\ &+ \mathbf{n}_\Gamma \cdot \nabla (|\nabla \psi_0| - 1) \delta(\alpha) \\ &- \kappa (|\nabla \psi_0| - 1) \delta(\alpha). \end{aligned} \quad (33)$$

Since  $\text{sign}[\mathbf{n}_\Gamma \cdot \nabla \delta(\alpha)] = -\text{sign}[\psi_0]$ , the first term on the RHS of equation (33) resembles the term in the re-initialization equation of the signed distance function introduced by Sussman et al. [10, 11]. The second RHS term in equation (33) contains information about the spatial distribution of a difference between

$|\nabla\psi_0(\alpha)|$  and the solution to the eikonal equation  $|\nabla\psi_0| = 1$ . The third RHS term in equation (33) contains the interface curvature  $\kappa$  and expresses its influence on the pair of re-initialized functions  $\alpha(\psi_0)$  and  $\psi_0(\alpha)$ . Re-initialization of  $\alpha(\psi_0)$  and  $\psi_0(\alpha)$  in equations (32)-(33) is restricted to the region of support of  $\delta(\alpha)/\epsilon_h$ , and thus it is localized in the vicinity of the interface  $\Gamma$ . We emphasize that the solution to equation (1) allowing re-initialization of the level-set function  $\alpha(\psi_0)$  is mathematically equivalent to the solution to equations (32) or (33) allowing re-initialization of  $\psi_0(\alpha)$ .

### 5.1. Determination of the $\gamma$ value

Shukla et al. in [2] and Tiwari et al. in [4] set the value of the constant  $\gamma$  in equation (8) to  $\gamma = 0.1$ . They argue that this value is justified because when  $\gamma \rightarrow 0$  the mapping function given by equation (8) tends to  $\psi_1 \rightarrow 1/2$  as shown in Appendix A.

In this section, we investigate numerically how to select the value of the constant  $0 < \gamma \ll \Delta x$ . We want to find  $\gamma$  such that  $\psi_1(\alpha, \gamma)$  in Eq. (20) accurately approximates the signed distance function  $\psi_0(\alpha)$  and thus assures the solution to Eq. (1) with minimal error. During tests in this section, the number of grid nodes  $N_c = 128$  and the support width  $\epsilon_h = \Delta x/2$  are both kept constant.

In the beginning of this study we note that Eq. (30) could be considered as the condition which supplies the maximal value of the constant  $\gamma_{max} \approx 4\epsilon_h$ . However, to derive Eq. (20), the more stringent condition  $0 < \gamma \ll \Delta x$  is required; convergence of Eq. (1) with  $\gamma = \epsilon_h$  is depicted in Fig. 4.

Figure (4) presents convergence of the solutions to Eq. (1) in the case of re-initialization of the 1D regularized Heaviside function with different values of the constant  $\gamma$ . Errors in solutions to Eq. (1) are measured by the  $L_1$  norm defined by Eq. (9). The initial condition to Eq. (1) is given by Eq. (2) which is its stationary, analytical solution.  $|\nabla\alpha|$  in Eq. (1) is discretized with the mapping functions  $\psi_1(\alpha, \gamma)$  and  $\psi_0(\alpha)$ . In order to obtain convergence when  $\gamma < 10^{-6}$  the size of time step  $\Delta\tau = \epsilon_h$  was reduced to  $\Delta\tau = \epsilon_h/2$ . In the

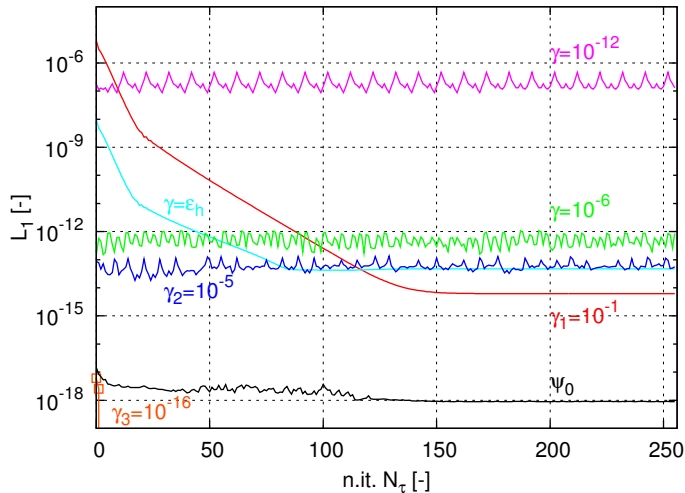


Figure 4: The influence of  $\gamma$  value in the mapping function  $\psi_1(\alpha, \gamma)$  on convergence of the solution to Eq. (1) during re-initialization of the 1D regularized Heaviside function.  $L_1$  norms are defined by Eq. (9).

present test case, the interface  $x_\Gamma = 0.5 m$  is localized exactly between the two neighboring control volumes  $x_P, x_F$ .

When  $\gamma_1 = 0.1$ , one needs about  $N_\tau \approx 140$  time steps to achieve the stationary solution. Similar to convergence with the exact signed distance function  $\psi_0(\alpha)$ , the most rapid convergence rate and the smallest error is obtained when  $\gamma_2 = 10^{-5}$ . For  $\gamma_2 < 10^{-5}$ , the error of the solution to equation (1) increases, albeit remains on a constant level. When  $\gamma_3 = 10^{-16}$ , the solver needs only two iterations and numerical zero is achieved as shown in Fig. 4. We suspect the increment of the error level is a numerical effect associated with accuracy of the *Fortran* compiler (all real variables in the Fastest solver are declared in double precision).

In figure 5 we compare the signed distance functions reconstructed using Eqs. (3) and (20) from the mapping functions  $\psi_0(\alpha)$  and  $\psi_1(\alpha, \gamma_2)$ ,  $\psi_1(\alpha, \gamma_3)$  after  $N_\tau = 256$  re-initialization steps. When  $\gamma_3 = 10^{-16}$ , the reconstructed signed distance function  $\psi'_0(\psi_1(\alpha, \gamma_3))$  has a staircase shape due to the existence of numerical errors in computation of high-order roots in Eq. (8), see Fig. 5(b).

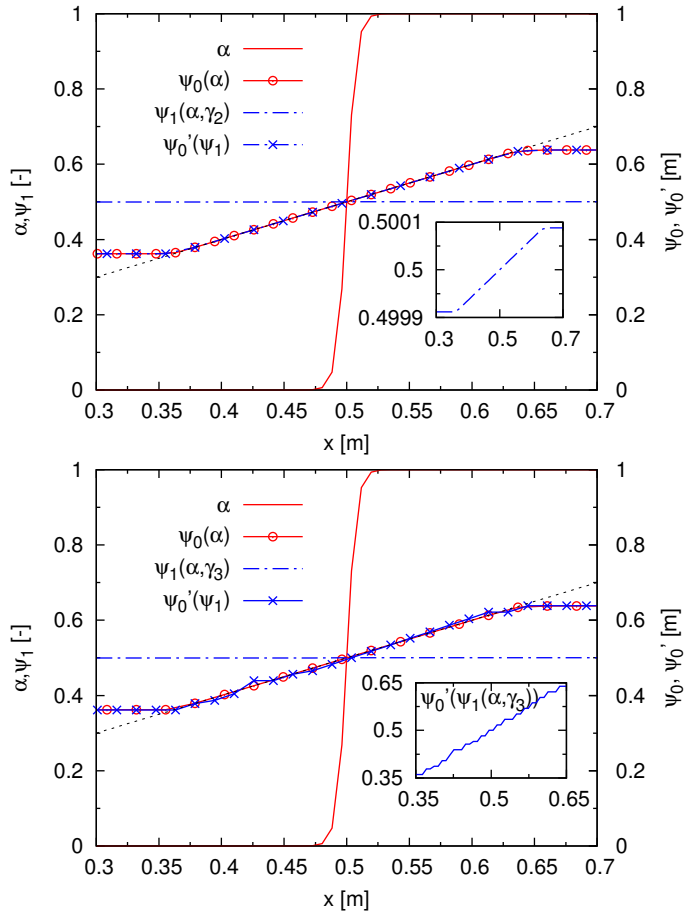


Figure 5: The comparison of signed distance functions reconstructed from  $\psi_1(\alpha, \gamma)$  with Eq. (20) after  $N_\tau = 256$  re-initialization steps (a)  $\gamma_2 = 10^{-5}$ , (b)  $\gamma_3 = 10^{-16}$  with  $\psi_0(\alpha)$  obtained using Eq. (3). The lines with symbols are plotted every second or third point to improve clarity in presentation of the results.

The latter result is empirical confirmation that the increment of  $L_1$  norm levels, observed in Fig. 4 when  $\gamma < \gamma_2 = 10^{-5}$ , has numerical origin. In figure 5(a), we observe that the signed distance function  $\psi_0'$  reconstructed from  $\psi_1(\alpha, \gamma_2)$  using equation (20) is identical with  $\psi_0(\alpha)$  obtained using equation (3).

### 5.2. Determination of the allowable interface width $\epsilon_h$

In the previous sections we have chosen  $\epsilon_h = \Delta x/2$  to set the support width of  $\delta(\alpha)/\epsilon_h$ , as this value is also used in the literature [1, 2, 4, 5, 15, 16]. However, at the beginning of Section 5 it was mentioned that other than the signed distance function  $\psi_0(\alpha)$ , the Heaviside function  $H(\psi_0)$  is the stationary solution to Eq. (32) as well. Subsequently, we will demonstrate how this feature of Eq. (32) is preserved by the present numerical scheme which does not use flux limiters or higher-order essentially non-oscillatory schemes (see Appendix B for details).

The lack of flux limiters in the present discretization of the re-initialization equation and employment of the second-order flux limiters only during the advection step may be an advantage, as the artificial deformations of the interface may be avoided. A deformation of the interface due to a *minmod* flux limiter was observed in [4] during re-initialization of  $\alpha(\mathbf{x}, t)$  with Eq. (4). The interface-grid lines alignment during advection is a known deficiency in compressive high-resolution schemes which use down-wind to maintain sharpness of the interface, and switch between higher and lower order differencing schemes to preserve its smoothness [19, 20, 21, 22]. Moreover, the numerical artifacts described above cannot be accepted during the reliable implementation of physical models based on the variable relaxation velocity  $C(\mathbf{x}, t)$ , and the variable variance  $\epsilon_h(\mathbf{x}, t)$  in Eq. (1). A good example of the physical model requiring abovementioned features of the numerical scheme, is the statistical model for the ensemble averaged description of interactions between the gas-liquid interface and turbulence [23, 24, 25].

Since in Eq. (20) we have shown that  $\psi_0 \approx \psi'_0$  for  $0 < \gamma \ll \Delta x$ , in this section, for brevity, we use only  $\psi_0$  for the discretization of  $|\nabla\alpha|$  in Eq. (1). In order to investigate the influence of  $\epsilon_h < \Delta x/2$  on convergence to the re-initialization equation, we carry out the same test as in the previous section with  $N_c = 128$  and with the initial condition given by Eq. (2). In the present case, the position of the interface is set to  $x_\Gamma = 0.6 m$ , and thus  $\Gamma$  is not localized exactly between two neighboring grid nodes  $x_P, x_F$ . Additionally,  $\epsilon_h = \Delta x/M$  where

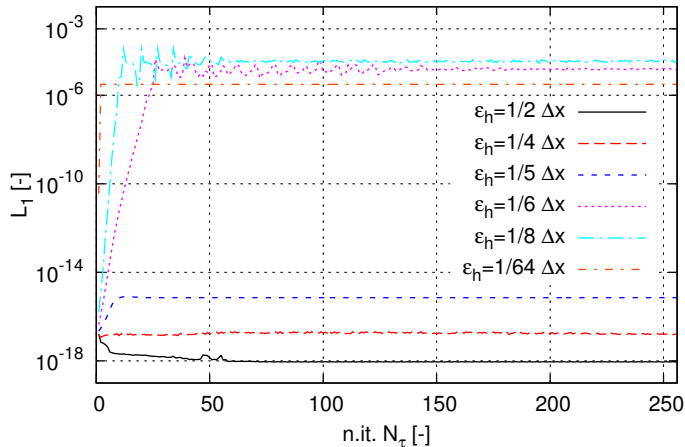


Figure 6: The impact of the variable  $\delta(\alpha)/\epsilon_h$  support width  $\epsilon_h = \Delta x/M$  where  $M \leq 16$ , on convergence of the solution to the re-initialization equation (32). Error is measured by  $L_1$  norm defined by Eq. (9).

$M \geq 2$  is an arbitrary integer number, the time step size is set to  $\Delta\tau = \epsilon_h/2$ .

In Fig. 6, convergence of the solution to Eq. (32) with a varying width of the interface  $\epsilon_h = \Delta x/M$  can be observed. The  $L_1$  norm defined by Eq. (9) remains approximately constant for  $M = 2, 4, 5$  and increases rapidly for  $M = 6, 8, 64$ . This increment, however, does not lead to the divergence of the present numerical solutions, we observe such behavior also when  $M = 16, 32$  ( $L_1^M < 10^{-4}$ ). The observed increment in the  $L_1$  norm magnitude is related to the finite resolution of the computational grid and the selected time step size  $\Delta\tau$ . We found that errors of the solutions to Eq. (1) remain smaller than the truncation error ( $L_1^M < 10^{-16}$ ) when  $\Delta\tau = \Delta x/2^M$  and  $M = 2, \dots, 8$ . The explanation of this fact is straightforward if one notices that in Eq. (32) for  $\epsilon_h \rightarrow 0$  the value of  $\nabla\delta(\alpha) = (1 - 2\alpha)\nabla\alpha$  increases when  $x \neq x_\Gamma$ . For practical reasons, later in this section we use  $\Delta\tau = \epsilon_h/2$ . In such case, the errors increase with decreasing  $\epsilon_h = \Delta x/M$  which follow from oscillations of the signed distance function  $\psi_0$ , see figures 7(b) and 8.

In the present test case it is found that if  $\epsilon_h = \Delta x/128$  then  $\delta(\alpha) = \alpha(1 - \alpha) = 0$  since in the given grid  $\forall x_i \leq x_P : \alpha_i = 0$  and  $\forall x_i \geq x_F : \alpha_i = 1$

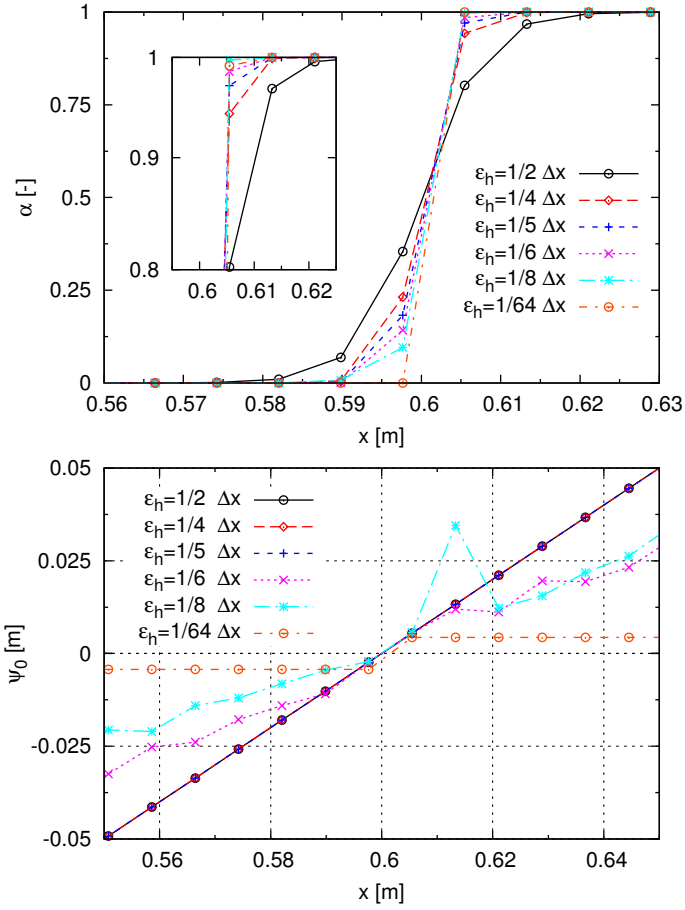


Figure 7: The influence of the variable  $\delta(\alpha)/\epsilon_h$  support width:  $\epsilon_h = \Delta x/M$  where  $M \leq 16$  on convergence to the solution to Eq. (32), (a)  $\alpha(\psi_0)$ , (b)  $\psi_0(\alpha)$  after  $N_\tau = 256$  re-initialization steps, the interface  $\Gamma$  is localized at  $x_\Gamma = 0.6$  m.

where  $x_P, x_F$  are the two neighboring grid points closest to the interface position  $x_\Gamma = 0.6$  m. Since  $\delta(\alpha) = 0$  in each point of the domain only when  $\alpha(\psi_0) = H(\psi_0)$ , the Heaviside function  $H(\psi_0)$  is the numerical solution to Eq. (32) as well.

The results presented in Fig. 7 show the support width of  $\delta(\alpha)/\epsilon_h$  is restricted by the accuracy of reconstruction of the level-set functions  $\alpha(\psi_0)$  and  $\psi_0(\alpha)$ . In order to accurately calculate gradient of  $\alpha(\psi_0)$ , one needs at least four

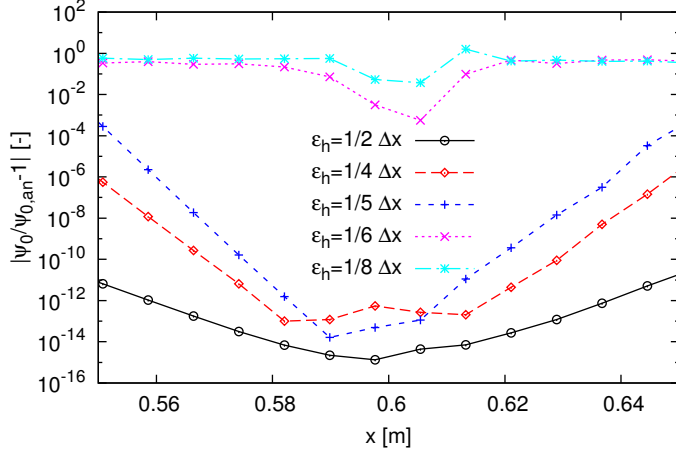


Figure 8: The impact of the variable  $\delta(\alpha)/\epsilon_h$  support width  $\epsilon_h = \Delta x/M$  where  $M \leq 8$  on the distribution of the error  $|\psi_0/\psi_{0,an} - 1|$ , where  $\psi_{0,an} = x - x_\Gamma$  and  $x_\Gamma = 0.6 m$ ,  $\psi_0(\alpha)$  is the signed distance function after  $N_\tau = 256$  re-initialization steps.

points around the interface  $\Gamma$  with correctly predicted values of  $\psi_0(\alpha)$ . In the 1D study presented here, this condition is satisfied when  $M \leq 4$  in  $\epsilon_h = \Delta x/M$  (compare results in figures 7-8).

Now, we can compare features of this new re-initialization equation with properties of the stationary solution to the phase-field equation which was investigated by Sun and Beckermann in [7]. The main difference lies in the fact that the stationary solution to the phase-field equation is always given by the regularized Heaviside function represented by the hyperbolic tangent profile; see formulation of the phase field equation in [7]. For this reason, in [7] it is recommended to use about 5 – 6 grid points to accurately reconstruct  $\alpha(\mathbf{x}, t)$ . In the present method when  $\epsilon_h \rightarrow 0$ , the numerical solution to Eq. (32) is given by the Heaviside function  $\alpha(\psi_0) = H(\psi_0)$  because in such case  $\delta(H) = 0$  on the given grid, and thus  $\partial\alpha/\partial\tau \equiv 0$  in Eq. (32). In subsequent sections, we investigate how the selection of the interface width  $\epsilon_h$  affects re-initialization of the interface  $\Gamma$  and computation of its curvature  $\kappa$ .

### 5.3. Interpretation of results

Let us now shortly summarize ideas introduced in the previous sections. Up to now the two discretizations of  $|\nabla\alpha|$  in Eq. (1) were introduced:  $|\nabla\alpha| = \zeta^2 \delta(\alpha)^{1-\gamma} / \gamma |\nabla\psi_1|$  and  $|\nabla\alpha| = \delta(\alpha) / \epsilon_h |\nabla\psi_0|$ , see Eq. (23) and Eq. (27) respectively. These two discretizations are equivalent when  $0 < \gamma \ll \Delta x$ , as shown by equations (20), (30) and in Fig. 5. The discretization of  $|\nabla\alpha|$  with Eq. (27) is free from round-off errors and is faster than the equivalent discretization with Eq. (23); in the latter case, higher-order roots of  $\alpha(\psi_0)$  must be calculated, see Eq. (8).

With these facts, we can now explain why equation (1) is solved with the largest accuracy when the mapping functions  $\psi_0(\alpha)$  or  $\psi'_0(\psi_1(\alpha, \gamma_2))$  are used for approximation of  $|\nabla\alpha|$ . Since  $\psi_0 \approx \psi'_0$  is the signed distance function  $|\nabla\psi_0(\alpha)| \approx |\nabla\psi'_0(\psi_1(\alpha, \gamma_2))| = 1$ , the right-hand sides in equations (32) and (33) are equal to zero when the initial condition to Eq. (1) is given by Eq. (2). This occurs regardless of  $\kappa$  values and explains the rapid convergence of the solution to Eq. (1) to a steady state as it is depicted in Figs. 4 and 6. Therefore, the simplification of Eq. (1) to Eq. (4) put forward by Shukla et al. in [2] is justified only when  $|\nabla\alpha| = \delta(\alpha) / \epsilon_h |\nabla\psi_0|$  where  $\psi_0$  is the signed distance function. When  $\psi_0(\alpha) \approx \psi'_0(\psi_1(\alpha, \gamma_2))$  is not the signed distance function, for example, due to  $\alpha(\psi_0)$  deformations during advection, the right-hand sides in Eqs. (32) and (33) are not equal to zero and the re-initialization process will begin.

In Section 5.2 we have shown that the stationary solution to Eq. (32) is also given by the Heaviside function  $H(\psi_0)$ . This distinguishes the new re-initialization method from re-initialization of the signed distance function put forward by Sussman et al. [10, 11] and the solution to the phase-field equation investigated by Sun and Beckermann [7]. In the 1D case, this feature of equation (32) allows decreasing the interface width up to  $\epsilon_h = \Delta x/4$  without large influence on the accuracy of reconstruction of the corresponding  $\alpha(\psi_0)$  and  $\psi_0(\alpha)$  functions as shown in Figs. 7 – 8. The latter result suggests that for  $K$  dimensional problems  $\epsilon_h = \sqrt{K}\Delta x/4$ , where  $K = 1, 2, 3$ . In [1] and in works

that followed, the interface width is set to  $\epsilon_h \geq \Delta x/2$  and it is reported that solutions of the re-initialization equation (1) are not stable when  $\epsilon_h < \Delta x/2$ . The new form of the re-initialization equation (1) given by equation (32) provides both the explanation and the solution to this problem.

Finally, we recall when  $\epsilon_h \rightarrow 0$  then  $\alpha(\psi_0) \rightarrow H(\psi_0)$ ,  $\delta(\alpha)/\epsilon_h \rightarrow \delta(\psi_0)$  and  $\partial\alpha/\partial\tau \equiv 0$  in equation (32). In this case, the advection equation of the conservative level-set function

$$\frac{\partial\alpha(\psi_0)}{\partial t} + w_i \frac{\partial\alpha(\psi_0)}{\partial x_i} = \frac{\delta(\alpha)}{\epsilon_h} \left[ \frac{\partial\psi_0(\alpha)}{\partial t} + w_i \frac{\partial\psi_0(\alpha)}{\partial x_i} \right] = 0, \quad (34)$$

becomes the advection equation of the phase indicator function  $H(\psi_0)$  which is discretized in the VOF family of methods,  $w_i$  in equation (34) is the  $i$ -th component of the interface velocity. Equation (34) shows that advection of the phase indicator function  $H(\psi_0)$  is equivalent to advection of the signed distance function  $\psi_0$  localized within the support of the Dirac's delta function  $\delta(\psi_0)$ . When  $\epsilon_h \neq 0$ , equation (34) describes advection of  $\alpha(\psi_0)$  and advection of  $\psi_0(\alpha)$  which is localized within the support of  $\delta(\alpha)/\epsilon_h$ . Equation (34) is valid in the whole domain of the solution unlike the transport equation of  $\psi_0(\mathbf{x}, t)$  derived in [10], valid only at the interface  $\Gamma$  ( $w_i \neq 0$  when  $x_i \in \text{supp}[\delta(\psi_0)]$  and  $w_i = 0$  elsewhere).

## 6. Numerical experiments

In the following sections, we investigate the rates of convergence and assess numerical errors during re-initialization of both the conservative level-set function  $\alpha(\psi_0)$  and the signed distance function  $\psi_0(\alpha)$ . Re-initialization is performed using Eq. (32) which is equivalent to Eq. (1) when  $|\nabla\alpha|$  is discretized with the signed distance function  $\psi_0$  or its approximation  $\psi'_0$ , see Eq. (3) and Eq. (20), respectively. In particular, we are interested in the case when the interface  $\Gamma$  is stationary,  $\epsilon_h = \sqrt{K}\Delta x/4 < \Delta x/2$  where  $K = 1, 2, 3$  is the dimension of the problem, and the number of re-initialization steps  $N_\tau \gg 1$ . In order to present properties of the new re-initialization method in a broader context, several advection test cases, where equations (32) and (34) are solved alongside, are

performed. The numerical errors during computation of  $\alpha(\psi_0)$  derivatives are measures of artificial deformations of the interface  $\Gamma$  due to a re-initialization process. In the next sections, their identification is our main concern.

### 6.1. Re-initialization of stationary interfaces

#### 6.1.1. Regularized Heaviside function

In figures 2 and 3 the solutions to equation (1) with the mapping function  $\psi_1(\alpha, \gamma_1)$  after  $N_\tau = 1$  re-initialization steps were illustrated, therein the width of the interface is set to  $\epsilon_h = \Delta x/2$  and the time step  $\Delta\tau = D/C^2 = \epsilon_h$ . In what follows, we discuss the results obtained with the same numerical setup as in section (2) but after  $N_\tau = 256$  re-initialization steps. The results presented below are obtained with  $\psi_1(\alpha, \gamma_1)$  where  $\gamma_1 = 0.1$ , and with the new mapping functions  $\psi_0(\alpha)$  and  $\psi_1(\alpha, \gamma_2)$  where  $\gamma_2 = 10^{-5}$ , see Sec. 5.1.

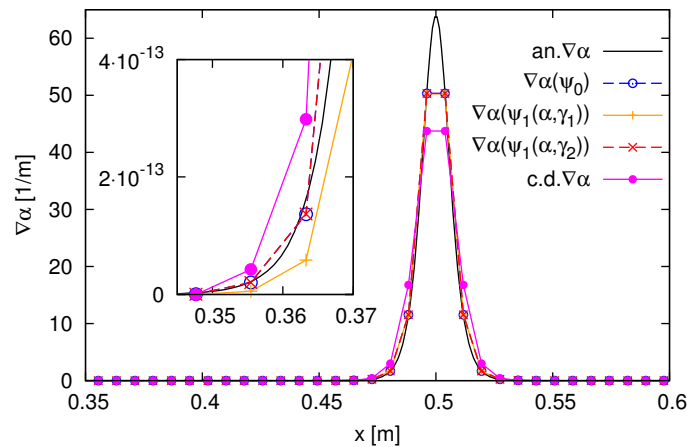


Figure 9: The comparison of exact  $\nabla\alpha$  (black solid line) with its numerical approximations after  $N_\tau = 256$  re-initialization steps of the 1D regularized Heaviside function.  $|\nabla\alpha|$  in Eq. (1) is discretized using the mapping functions:  $\psi_0(\alpha)$ ,  $\psi_1(\alpha, \gamma_1)$  or  $\psi_1(\alpha, \gamma_2)$  where  $\gamma_1 = 0.1$ ,  $\gamma_2 = 10^{-5}$  see Eq. (27) and Eq. (23), respectively. c.d. $\nabla\alpha$  denotes gradient of  $\alpha(\mathbf{x}, t)$  computed using the central differencing scheme.

In figures 9 and 10, approximations to the first component of  $\nabla\alpha(\psi_0)$  calculated using Eq. (23) and Eq. (27) are presented. In figure 9, it is observed

that both  $\psi_0(\alpha)$  and  $\psi_1(\alpha, \gamma_2)$  reconstruct the bell-like shape of the first-order analytical derivative of Eq. (2) better than  $\psi_1(\alpha, \gamma_1)$ ; this result is expected in the light of Eq. (20). The distributions of the  $L_1(\nabla\alpha)$  norms in Fig. 10 confirm these observations. We note that  $\nabla\alpha$  is approximated with the smallest error in the neighborhood of the interface located at  $x_\Gamma = 0.5 m$ .

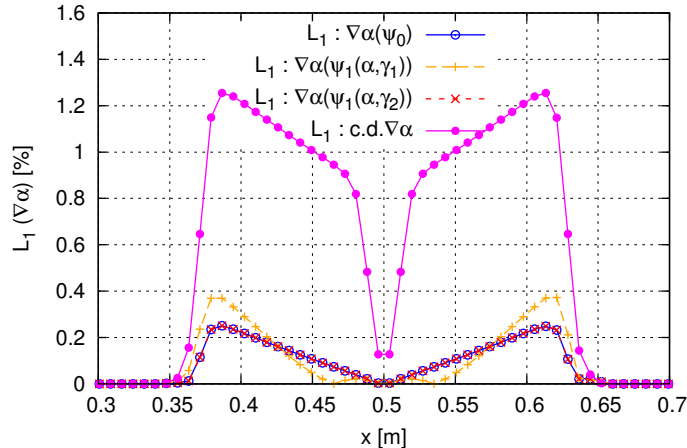


Figure 10: Distributions of the  $L_1(\nabla\alpha)$  norms defined by Eq. (10) after  $N_\tau = 256$  re-initialization steps of the 1D regularized Heaviside function.  $L_1(\nabla\alpha)$  is calculated using the  $\nabla\alpha$  discretizations with the mapping functions:  $\psi_0(\alpha)$ ,  $\psi_1(\alpha, \gamma_1)$  and  $\psi_1(\alpha, \gamma_2)$  where  $\gamma_1 = 0.1$ ,  $\gamma_2 = 10^{-5}$ , c.d.  $\nabla\alpha$  denotes the central differencing gradient  $\alpha(\mathbf{x}, t)$  approximation.

The distributions of the errors after  $N_\tau = 256$  re-initialization steps in the case of  $\psi_0(\alpha)$  and  $\psi_1(\alpha, \gamma_2)$  are similar to the error distribution of  $\psi_1(\alpha, \gamma_1)$  after  $N_\tau = 1$  re-initialization steps (compare Fig. 3 and Fig. 10). In the case of  $\psi_1(\alpha, \gamma_1)$ , the  $L_1(\nabla\alpha)$  norm (the numerical gradient approximation within Eq. (10)) is varying during the integration of Eq. (1) in time  $\tau$ . This artificial deformation of  $\nabla\alpha$  in time  $\tau$  is the main reason for longer convergence of Eq. (1) to the steady state as shown in Fig. 4.

Next, we discuss the accuracy of computations of the second-order spatial derivatives of the level-set function  $\alpha(\psi_0)$ . In Section 4, the formulas for  $\alpha_{,ij}$  using  $\psi_1(\alpha, \gamma)$  and  $\psi_0(\alpha)$  were derived, see equations (26) and (28), respectively.

To compute the second-order spatial derivatives of  $\alpha(\psi_0)$ , one needs both the second and first order derivatives of the mapping functions  $\psi_0(\alpha)$  or  $\psi_1(\alpha, \gamma)$ . In our code they are calculated using the discrete Gauss theorem equivalent to

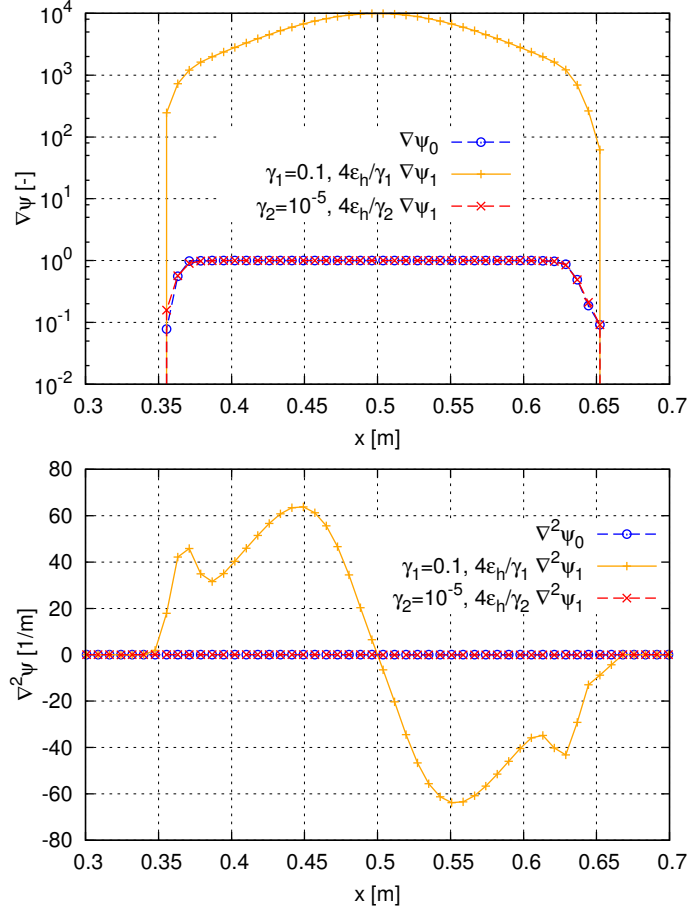


Figure 11: The comparison of (a)  $\nabla\psi$ , (b)  $\nabla^2\psi$  obtained after  $N_\tau = 256$  re-initialization steps of the 1D regularized Heaviside function.

the second-order accurate central difference gradient approximation, see [26, 27].

In figure 11(a) we compare the relation between  $\nabla\psi_0(\alpha)$  and  $4\epsilon_h/\gamma\nabla\psi_1(\alpha, \gamma)$ , provided by Eq. (21). One notes when  $\psi_1(\alpha, \gamma_1)$  is used, the mapping function is not the signed distance function since  $|4\epsilon_h/\gamma_1\nabla\psi_1(\alpha, \gamma_1)| \neq 1$ . On the other hand, gradient calculated using  $\psi_0(\alpha)$  and  $\psi'_0(\psi_1(\alpha, \gamma_2))$  gives  $|\nabla\psi_0| \approx |\nabla\psi'_0| =$

1 inside the support of  $\delta(\alpha)/\epsilon_h$ ; with this, correctness of equations (20) and (21) is confirmed.

In figure 11(b), the second-order spatial derivatives of the mapping functions  $\psi_0(\alpha)$  and  $\psi_1(\alpha, \gamma)$  are compared. As  $\psi_1(\alpha, \gamma_1)$  does not approximate the signed distance function, its second-order derivative is not equal to zero everywhere in the computational domain, see Eq. (22). Since  $\psi_0(\alpha)$  is the signed distance function and  $\psi'_0(\psi_1(\alpha, \gamma_2))$  is its approximation, see Eq. (20), their second derivatives are equal to zero when  $x \in \text{supp}[\delta(\alpha)/\epsilon_h]$ . Consequently, the accuracy of approximation of the second-order derivatives using Eq. (26) and Eq. (28) is very similar to accuracy achieved when the first-order derivatives are computed with Eq. (23) and Eq. (27); compare results in Fig. 10 and in Fig. 13(a).

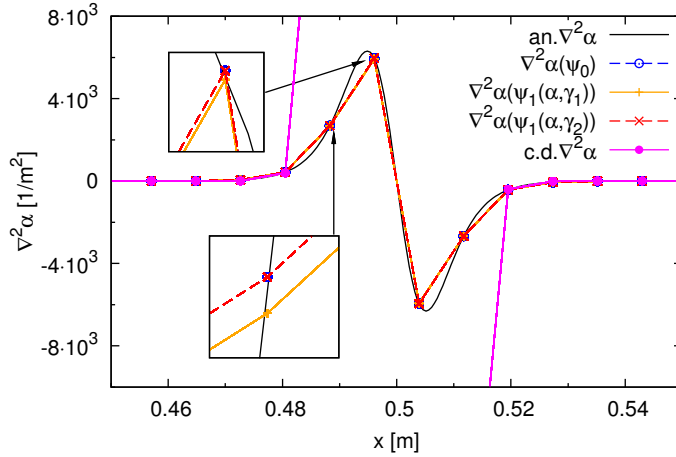


Figure 12: The comparison of  $\nabla^2\alpha(\psi)$  after  $N_\tau = 256$  re-initialization steps of the 1D regularized Heaviside function obtained with Eq. (26) or Eq. (28) with the second-order derivative calculated analytically from Eq. (2) (solid-black line) and the central difference (c.d.  $\nabla^2\alpha$ ) approximation.  $\psi$  is one of the mapping functions:  $\psi_0(\mathbf{x}, t)$ ,  $\psi_1(\alpha, \gamma_1)$  or  $\psi_1(\alpha, \gamma_2)$ .

In figures 12-13, the non-zero terms in  $\nabla^2\alpha$ , calculated with Eq. (26) and Eq. (28), are compared with analytically calculated second-order derivative of Eq. (2) and its central difference approximation. The first observation in Fig. 12 is

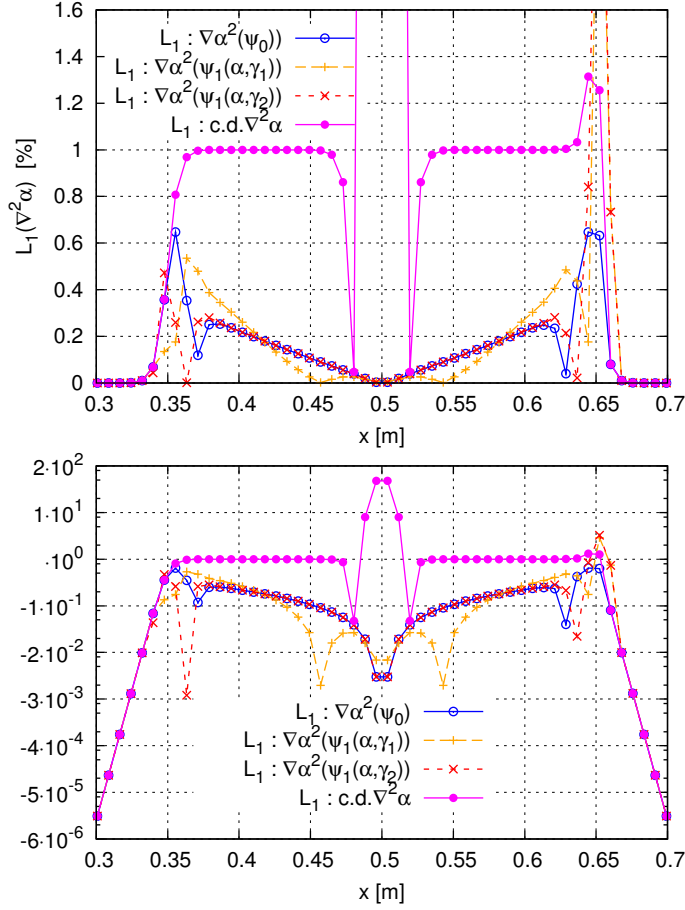


Figure 13: The comparison of  $L_1 (\nabla^2 \alpha(\psi))$  norms after  $N_\tau = 256$  re-initialization steps of the 1D regularized Heaviside function.  $\psi$  is one of the mapping functions:  $\psi_1(\alpha, \gamma_1)$ ,  $\psi_1(\alpha, \gamma_2)$  or  $\psi_0(\alpha)$ ,  $L_1$  norm is defined by Eq. (10). c.d.  $\nabla^2 \alpha$  denotes the second-order derivative computed using the central differencing method, figures (a) and (b) present the same results but the Y-axis scales are different.

a very good reconstruction of the second-order derivative in the case of all three mapping functions; see also Fig. 13 where the distribution of  $L_1 (\nabla^2 \alpha)$  error defined by Eq. (10) is depicted. As expected, the second order derivatives of  $\alpha(\psi_0(\mathbf{x}, t))$  calculated with  $\psi_1(\alpha, \gamma_2)$  and  $\psi_0(\alpha)$  are closest to each other and to the analytical solution. In Fig. 13, one notices when  $\psi_1(\alpha, \gamma_2)$  and  $\psi_0(\alpha)$  are used, the differences between these two approximations are visible only in

points where the jumps of  $\psi_1(\alpha, \gamma)$  with  $\epsilon = 0$  in Fig. 1 are present (about  $x = 0.35 m$  and  $x = 0.65 m$ ). Thus, oscillations observed in the  $L_1(\nabla^2\alpha)$  norm can be attributed to the truncation errors due to a floating point underflow.

In the light of the 1D re-initialization studies presented above we conclude that the most accurate discretization of  $|\nabla\alpha|$  in equation (1) is achieved with the mapping function  $\psi_0(\alpha)$ , see Eq. (27). This discretization is also the most natural one since the mapping between  $\psi_0(\alpha)$  and  $\alpha(\psi_0)$  is well defined by Eq. (3). We recall that after proper selection of the mapping function, Eq. (1) is equivalent to Eqs. (32) and (33) which are the conservative and non-conservative form of the re-initialization equation of the signed distance function  $\psi_0(\alpha)$  and the conservative level-set function  $\alpha(\psi_0)$ . Since equation (1) is solved accurately when  $x \in \text{supp}[\delta(\alpha)/\epsilon_h]$ , there is no need for an introduction of additional techniques in the present solution procedure, which reconstruct the signed distance function  $\psi_0$  in the vicinity of the interface  $\Gamma$ .

*Influence of initial conditions and the interface width on the convergence rate.*

In most of the previous examples, the interface  $\Gamma$  was localized exactly in-between neighboring control volumes  $x_P, x_F$ ; the width of the  $\delta(\alpha)/\epsilon_h$  support was set to  $\epsilon_h = \Delta x/2$  and equation (1) was initialized with its own analytical solution given by equation (2). However, during advection of the level-set functions  $\alpha(\psi_0)$  and  $\psi_0(\alpha)$ , the re-initialization equation (32) must handle more general initial conditions. For this reason, in what follows we study influence of the arbitrary interface location (here  $x_\Gamma = 0.6 m$ ), and the support width  $\epsilon_h$  on the convergence rate of  $\alpha(\psi_0)$  and its spatial derivatives during re-initialization of the 1D regularized Heaviside function.

In this study, the initial condition to Eq. (1) is not given by its analytical solution; at  $\tau = 0$  we set  $\epsilon_{h,0} = 2\epsilon_h$  and we consider two widths of the interface:  $\epsilon_h = \Delta x/2$  and  $\epsilon_h = \Delta x/4$ . The discretization of the 1D computational domain is the same as described in Sec. 6.1.1. For brevity, only the results obtained with  $\psi_0(\alpha)$  used in discretization of  $|\nabla\alpha|$  in Eq. (1) are presented in this section.

In figures 14-16 it is observed that the numerical solution to Eq. (1) converges

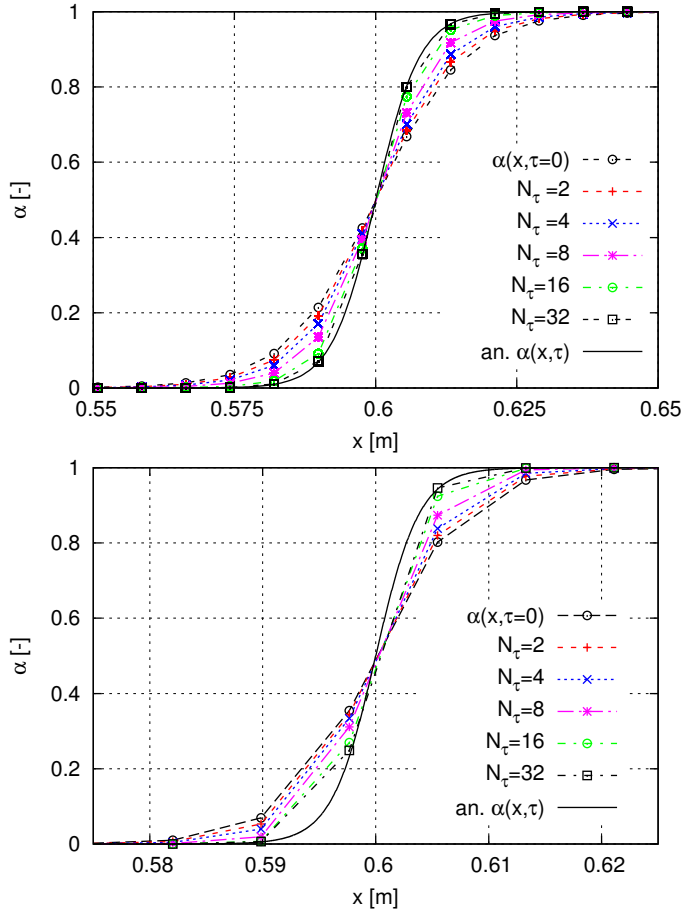


Figure 14: Convergence of the level-set function  $\alpha(\psi_0)$  towards its analytical solution,  $\alpha(\mathbf{x}, \tau = 0)$  is set using  $\epsilon_{h,0} = 2\epsilon_h$  where (a)  $\epsilon_h = \Delta x/2$ , (b)  $\epsilon_h = \Delta x/4$ , the time step size  $\Delta\tau = \epsilon_h/2$ .  $|\nabla\alpha|$  in Eq. (1) is discretized with  $\psi_0(\alpha)$ .

towards its analytical counterpart independent from the selected final support width of  $\delta(\alpha)/\epsilon_h$ . We emphasize that re-initialization of  $\alpha(\psi_0)$  with  $\epsilon_{h,0} = 2\epsilon_h$  is also possible when  $\epsilon_h = \Delta x/M$ . When  $M > 4$  the solution of Eq. (32) is convergent but the error level in the representation of  $\alpha(\psi_0)$  and  $\psi_0(\alpha)$  grows, see Fig. 17. As it is discussed in Section 5.2, this occurs due to finite spatial and temporal resolutions.

Since the interface  $\Gamma$  is not localized exactly in-between neighboring control

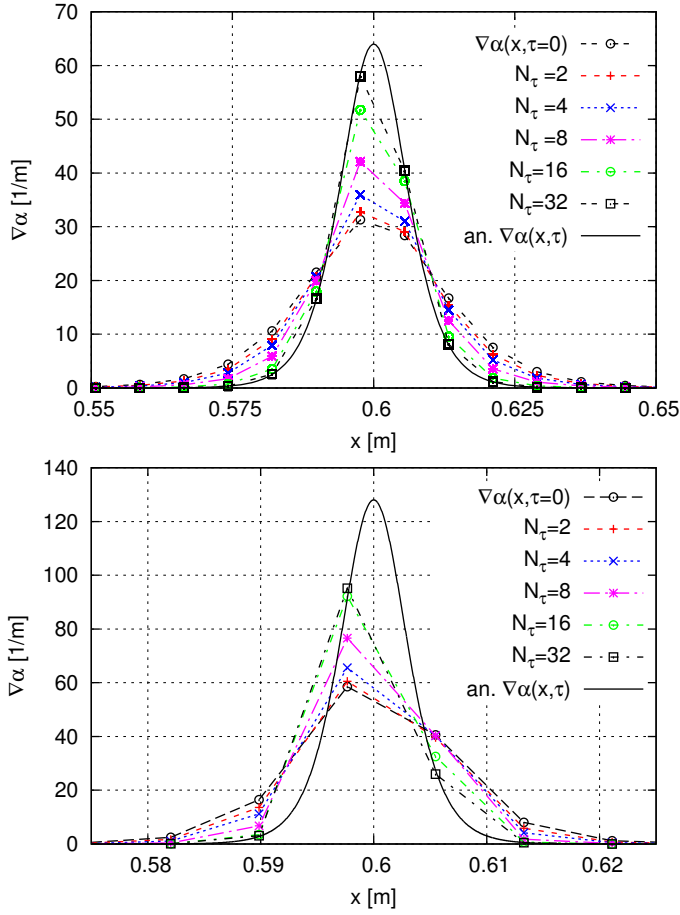


Figure 15: Convergence of  $\nabla\alpha(\psi_0)$  towards its analytical solution,  $\alpha(\mathbf{x}, \tau = 0)$  is set using  $\epsilon_{h,0} = 2\epsilon_h$  where: (a)  $\epsilon_h = \Delta x/2$ , (b)  $\epsilon_h = \Delta x/4$ , the time step size  $\Delta\tau = \epsilon_h/2$ .  $|\nabla\alpha|$  in Eq. (1) is discretized with  $\psi_0(\alpha)$ .

volumes  $x_P, x_F$ , obtained solutions are not symmetrical as depicted in Figs. 14 – 16. In spite of this, the shapes of the level-set function  $\alpha(\psi_0)$  and its first and second-order spatial derivatives are correctly reconstructed. We note that in the limit of  $N_\tau \rightarrow \infty$ , the present numerical solution to equation (32) tends to its stationary analytical solution given by equation (2) and its first and second order spatial derivatives. The discretizations of equation (1) presented in the extant literature do not guarantee convergence towards its stationary analytical

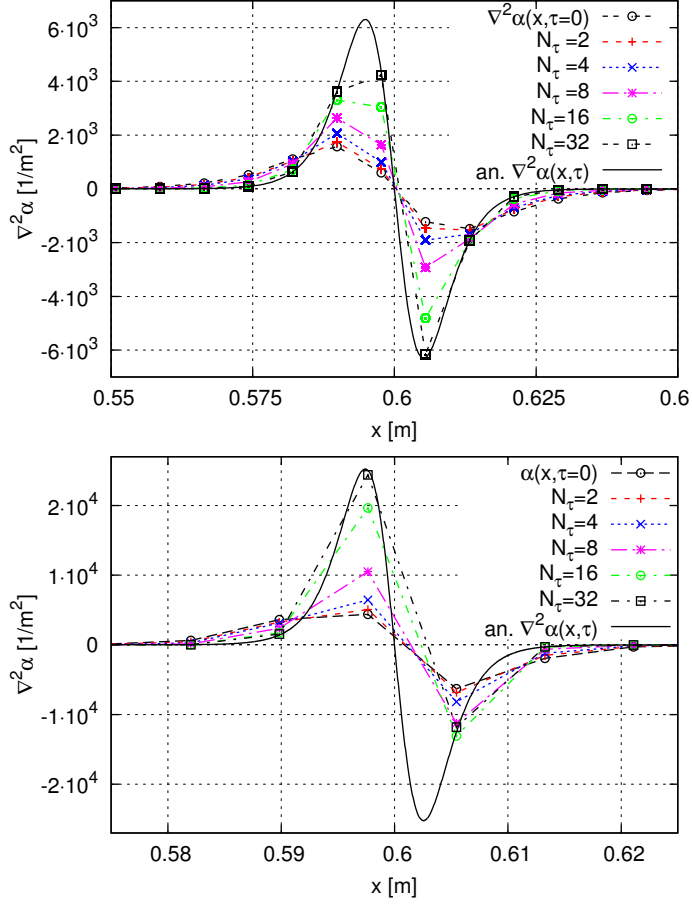


Figure 16: Convergence of  $\nabla^2\alpha(\psi_0)$  towards its analytical solution,  $\alpha(\mathbf{x}, \tau = 0)$  is set using  $\epsilon_{h,0} = 2\epsilon_h$  where: (a)  $\epsilon_h = \Delta x/2$ , (b)  $\epsilon_h = \Delta x/4$ , the time step size  $\Delta\tau = \epsilon_h/2$ .  $|\nabla\alpha|$  in Eq. (1) is discretized with  $\psi_0(\alpha)$ .

solution, artificial deformations of the interface  $\Gamma$  that emerge when  $N_\tau \gg 1$  are the result of this inconsistency.

### 6.1.2. Circular interface

In the case of the 1D regularized Heaviside function re-initialized in Section 6.1.1, equations (1) and (4) are equivalent since  $\kappa = -\nabla \cdot \mathbf{n}_\Gamma \equiv 0$ . In 2D or 3D cases that are discussed next,  $\kappa \neq 0$ . Choosing the mapping function as the signed distance function  $\psi_0(\alpha)$  allows us to write equation (1) in the form

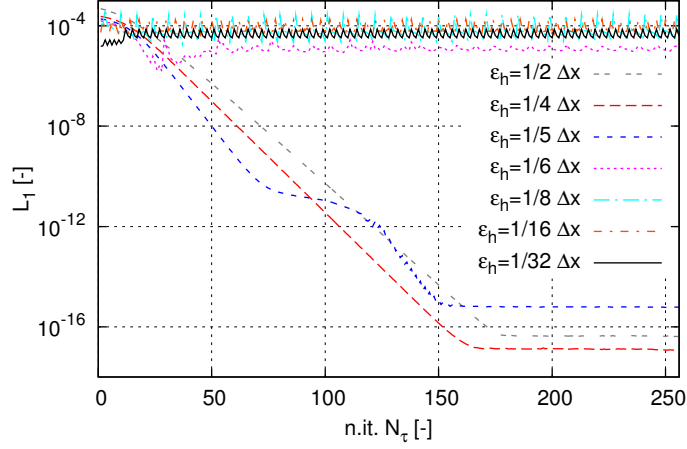


Figure 17: The  $L_1$  norms defined by Eq. (9) obtained during re-initialization of the 1D regularized Heaviside function  $\alpha(\psi_0)$  with Eq. (32) and the variable interface width  $\epsilon_h$ . The interface is located at  $x_\Gamma = 0.6 m$ , at  $\tau = 0$   $\epsilon_{h,0} = 2\epsilon_h$ ,  $\Delta\tau = \epsilon_h/2$ ,  $\epsilon_h = \Delta x/M$  and  $M = 2, \dots, 32$ .

of equations (32) or (33) and solve one of these equations without neglecting the influence of  $\kappa$  on the re-initialization process. When equation (1) is solved correctly, equation (3) that defines the signed distance function  $\psi_0(\alpha)$  holds; we use this fact in the present solution procedure.

In what follows, we assess influence of the selected mapping function and the interface width ( $\epsilon_h = \Delta x/2$  or  $\epsilon_h = \sqrt{2}\Delta x/4$ ) on the accuracy of approximations of  $\alpha(\psi_0)$  derivatives, see Eqs. (23) and (27) or Eqs. (26) and (28), respectively. These derivatives are used in calculation of the interface curvature  $\kappa$  according

to the formula

$$\begin{aligned}
\kappa &= (\alpha_1^2 \alpha_{22} + \alpha_2^2 \alpha_{11} + \alpha_1^2 \alpha_{33} + \alpha_3^2 \alpha_{11} + \alpha_2^2 \alpha_{33} + \alpha_3^2 \alpha_{22} \\
&\quad - 2\alpha_1 \alpha_2 \alpha_{12} - 2\alpha_1 \alpha_3 \alpha_{13} - 2\alpha_2 \alpha_3 \alpha_{23}) / |\nabla \alpha|^3 \\
&= \left\{ \psi_{0,1}^2 \left[ \psi_{0,22} + \frac{\psi_{0,2}^2}{\epsilon_h} (1 - 2\alpha) \right] + \psi_{0,2}^2 \left[ \psi_{0,11} + \frac{\psi_{0,1}^2}{\epsilon_h} (1 - 2\alpha) \right] \right. \\
&\quad + \psi_{0,1}^2 \left[ \psi_{0,33} + \frac{\psi_{0,3}^2}{\epsilon_h} (1 - 2\alpha) \right] + \psi_{0,3}^2 \left[ \psi_{0,11} + \frac{\psi_{0,1}^2}{\epsilon_h} (1 - 2\alpha) \right] \\
&\quad + \psi_{0,2}^2 \left[ \psi_{0,33} + \frac{\psi_{0,3}^2}{\epsilon_h} (1 - 2\alpha) \right] + \psi_{0,3}^2 \left[ \psi_{0,22} + \frac{\psi_{0,2}^2}{\epsilon_h} (1 - 2\alpha) \right] \\
&\quad - 2\psi_{0,1}\psi_{0,2} \left[ \psi_{0,12} + \frac{\psi_{0,1}\psi_{0,2}}{\epsilon_h} (1 - 2\alpha) \right] \\
&\quad - 2\psi_{0,1}\psi_{0,3} \left[ \psi_{0,13} + \frac{\psi_{0,1}\psi_{0,3}}{\epsilon_h} (1 - 2\alpha) \right] \\
&\quad \left. - 2\psi_{0,2}\psi_{0,3} \left[ \psi_{0,23} + \frac{\psi_{0,2}\psi_{0,3}}{\epsilon_h} (1 - 2\alpha) \right] \right\} / |\nabla \psi_0|^3, \tag{35}
\end{aligned}$$

which is written for the mapping function  $\psi_0(\alpha)$  and is valid when  $x_i \in \text{supp}[\delta(\alpha)/\epsilon_h]$ .

Unlike in the standard approach which uses only the signed distance function  $\psi_0$ , equation (35) contains terms that contribute to  $\kappa$  exclusively away from the interface  $\Gamma$ . These terms are multiplied by factor  $(1 - 2\alpha)$  and they vanish at  $\Gamma$ , i.e., when  $\alpha(\psi_0 = 0) = 1/2$ . At the interface  $\Gamma$  equation (35) reduces to  $\kappa$  definition given in [12].

In the following sections we investigate the convergence rate of the circular interface curvature on five gradually refined meshes  $m_i = 2^{4+i} \times 2^{4+i}$  where  $i = 1, \dots, 5$ . The initial condition to Eq. (1) is given by Eq. (2) where

$$\psi_0(\mathbf{x}, \tau = 0) = \left[ \sum_{i=1}^2 (x_i - x_{0,i})^2 \right]^{1/2} - R, \tag{36}$$

$(x_{0,1}, x_{0,2}) = (0.5m, 0.5m)$  denotes the center of the circle with the radius  $R = 0.2m$ . In this test case, the computational domain is quadratic box  $\Omega = \langle 0, 1 \rangle \times \langle 0, 1 \rangle$ , and the number of grid nodes depends on the size of the grid  $m_i$ .

*Convergence of the re-initialization equation.* In what follows, the convergence rate to the solution to Eq. (1) during  $N_\tau = 256$  re-initialization steps on grids  $m_i$ ,  $i = 1, \dots, 5$  is presented. We compare the results obtained with two  $\delta(\alpha)/\epsilon_h$  support widths:  $\epsilon_h = \Delta x/2$ ,  $\epsilon_h = \sqrt{2}\Delta x/4$ , where the time step size is  $\Delta\tau = C/D^2 = \epsilon_h$ . Unlike in the 1D case, the convergence rates and  $L_1$  norms on gradually refined grids are practically the same when  $\psi_1(\alpha, \gamma_2)$  and  $\psi_0(\alpha)$  mapping functions are used (compare results in figures 18(b)(d) and in figure 4). These results again confirm the correctness of the relation given by Eq. (20). In the case of  $\psi_0(\alpha)$ ,  $\psi_1(\alpha, \gamma_2)$  and for both interface widths  $\epsilon_h$  the stationary

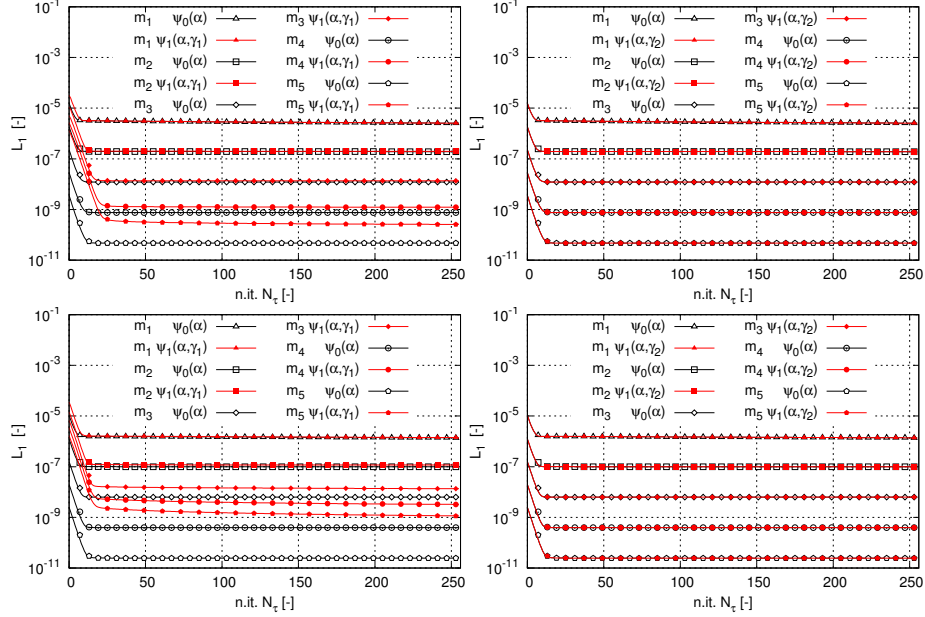


Figure 18: Convergence of the solution to Eq. (1) during re-initialization of the 2D circular interface,  $L_1$  norms defined by Eq. (9) are obtained for the mapping functions:  $\psi_1(\alpha, \gamma_1)$ ,  $\psi_1(\alpha, \gamma_2)$  and  $\psi_0(\alpha)$ , the interface width is set to  $\epsilon_h = \Delta x/2$  (top) and  $\epsilon_h = \Delta x\sqrt{2}/4$  (bottom),  $\Delta\tau = \epsilon_h$ , symbols correspond to every sixth or every twelfth iteration in time  $\tau$ .

solution is achieved after about  $N_\tau \approx 10$  iterations in time  $\tau$ . The integration of Eq. (1) with the mapping function  $\psi_1(\alpha, \gamma_1)$  requires about  $N_\tau \approx 25$  iterations

to achieve the steady state solution, see figures 18(a)(c). In this latter case, the convergence rate is lower and the error level is higher when compared with the results obtained with  $\psi_0(\alpha)$  and  $\psi_1(\alpha, \gamma_2)$ .

Lack of immediate convergence of the numerical solution to a steady state (as in the 1D case depicted in Fig. 4) is explained by additional numerical errors which are introduced to the solution of Eq. (1) during discretization process in the 2D case. The two sources of the numerical errors can be identified: the second-order discretization of the fluxes on the RHS of Eq. (1), and the computation of  $\psi_0(\alpha)$  gradients and normals to the interface  $\Gamma$  with the central-differencing scheme which is known to be mathematically exact approximation of the spatial derivatives only in the 1D case, see [26].

During numerical experiments it was found that differences between rates of convergence and their levels for the  $\psi_0(\alpha)$ ,  $\psi_1(\alpha, \gamma_2)$  and  $\psi_1(\alpha, \gamma_1)$  mapping functions are more pronounced when  $\Delta x/4 \leq \epsilon_h < \Delta x\sqrt{2}/4$  and  $\Delta\tau < D/C^2$ . For the sake of brevity, we subsequently use the time step size  $\Delta\tau = D/C^2 = \epsilon_h$  for the two different interface widths  $\epsilon_h = \Delta x/2$  and  $\epsilon_h = \Delta x\sqrt{K}/4$  where  $K = 2, 3$  for 2D or 3D problems, respectively.

*Computation of the circular interface curvature.* Next, we compute a numerical approximation  $\kappa'$  of the exact curvature  $\kappa$  using equation (35), and we investigate its convergence rate on five gradually refined grids after  $N_\tau = 256$  re-initialization steps when  $\epsilon_h = \Delta x/2$  or  $\epsilon_h = \sqrt{2}\Delta x/4$ . Since  $\alpha(\psi_0(\mathbf{x}, t))$  is the level-set function,  $\kappa'$  is calculated not only at the interface  $\alpha(\mathbf{x}_\Gamma, t) = 0.5$  but also at  $\alpha(\mathbf{x}^1, t) = 0.05$  and at  $\alpha(\mathbf{x}^2, t) = 0.95$ , see Fig. 19. The exact curvature  $\kappa_i$  of a circle on grid  $m_i$  at the interface  $\mathbf{x}_{i,\Gamma}$  is constant and equal to  $\kappa_i = 1/\mathcal{R}_i = 1/(|\mathbf{x}_{i,\Gamma} - \mathbf{x}_0|)$ .  $\mathcal{R}_i$  is the numerical approximation to  $R$  and is determined separately for  $\alpha(\psi_0)$ ,  $\psi'_0(\psi_1)$  and  $\psi_0(\alpha)$  on each grid  $m_i$ ,  $i = 1, \dots, 5$ , see Fig. 20. In the cases  $\alpha(\mathbf{x}_i^1, t)$  and  $\alpha(\mathbf{x}_i^2, t)$  curvatures are

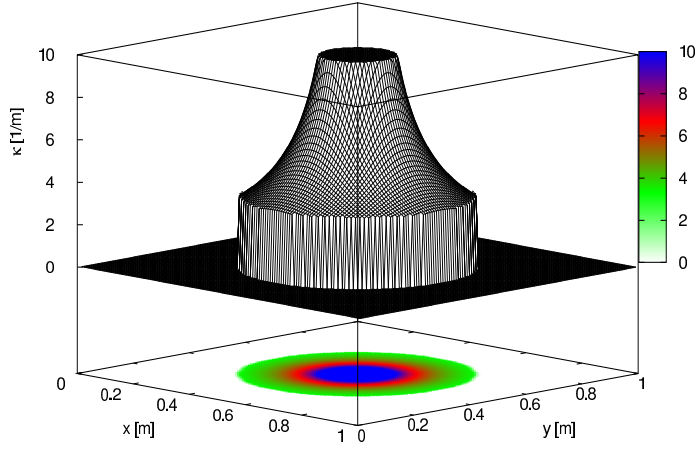


Figure 19: The curvature field  $\kappa_3'$  after  $N_\tau = 256$  re-initialization steps of the 2D circular interface obtained on the grid  $m_3$  with the mapping function  $\psi_0(\alpha)$ . The interface width is set to  $\epsilon_h = \Delta x/2$ .

defined by  $\kappa_1 = 1/(\mathcal{R}_i + r_i^1)$  and  $\kappa_2 = 1/(\mathcal{R}_i + r_i^2)$  where

$$r_i^1 = \epsilon_{h,i} \ln \left[ \frac{\alpha(\mathbf{x}_i^1, t) + \epsilon}{1 - \alpha(\mathbf{x}_i^1, t) + \epsilon} \right], \quad (37)$$

$$r_i^2 = \epsilon_{h,i} \ln \left[ \frac{\alpha(\mathbf{x}_i^2, t) + \epsilon}{1 - \alpha(\mathbf{x}_i^2, t) + \epsilon} \right], \quad (38)$$

$\epsilon_{h,i}$  depends on the grid size and  $\epsilon = 5 \cdot 10^{-16}$  is a small constant.

We note when the mapping function is used in discretization of Eq. (1), two representations of the interface  $\Gamma$  do exist. These two representations are given by:  $\alpha(\mathbf{x}_\Gamma, t) = 1/2$  and  $\psi_0'(1/2) = 0$  or  $\psi_0(1/2) = 0$ , and they are equivalent when  $\epsilon_h \rightarrow 0$ , see Fig. 20. For this reason the  $L_1^\kappa$  error is calculated as follows, first, the interface iso-lines are computed for each grid  $m_i$ :

1.  $\mathbf{x}_i^\alpha$  from  $\alpha(\mathbf{x}_\Gamma, t) = 1/2$ ,
2.  $\mathbf{x}_i^{\psi_0'}$  from  $\psi_0'(1/2) = 0$ , see Eq. (20),
3.  $\mathbf{x}_i^{\psi_0}$  from  $\psi_0(1/2) = 0$ , see Eq. (3).

Later, when we refer to sets of points representing the interface iso-lines we use the notation  $\mathbf{x}_i^\omega$  where  $\omega = \alpha, \psi_0'$  or  $\psi_0$ . Next, the value of the curvature

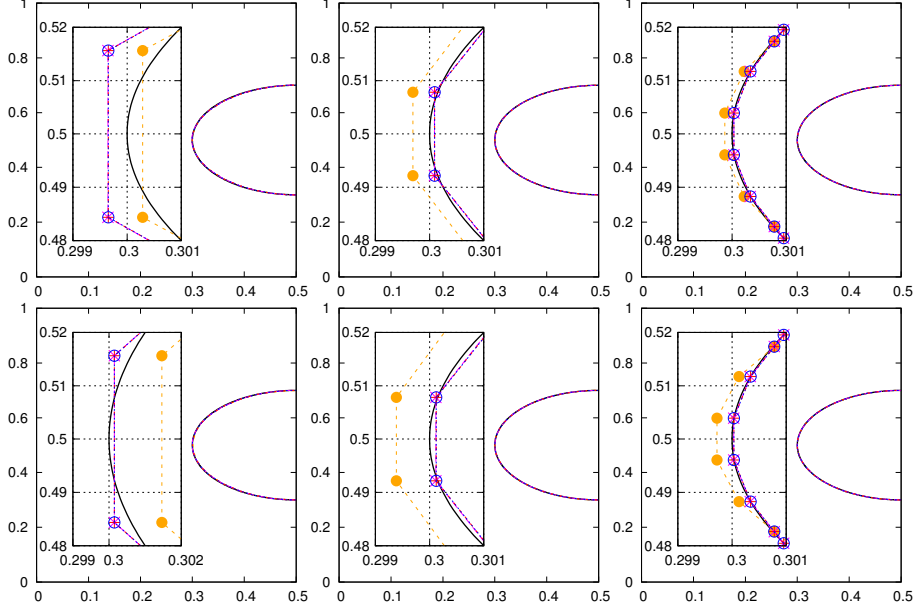


Figure 20: Convergence of different interface representations towards the analytical interface (black solid line) after  $N_\tau = 256$  re-initialization steps. The interface width is set to  $\epsilon_h = \Delta x/2$  (top) and  $\epsilon_h = \sqrt{2}\Delta x/4$  (bottom). The interface  $\Gamma$  is captured using: the regularized Heaviside function  $\alpha(\psi_0(\mathbf{x}, t))$  (solid orange dots), the signed distance functions  $\psi'_0(\psi_1(\alpha, \gamma))$  where  $\gamma_1 = 0.1$  (red crosses),  $\gamma_2 = 10^{-5}$  (magenta stars), and  $\psi_0(\alpha)$  (void dark blue dots) on grids:  $m_1, m_2, m_3$  from left to right.

$\kappa_i = 1/\mathcal{R}_i = 1/\max(|\mathbf{x}_i^\omega - \mathbf{x}_0|)$  is computed, using equations (37) and (38) away from the interface  $\Gamma$ . Now, from a given  $\kappa'_i$  field that is a numerical approximation of the curvature  $\kappa_i = 1/\mathcal{R}_i$ , the iso-contours given by the sets of points  $\mathbf{x}_i^{\omega, \kappa'}$  are determined on each grid  $m_i$  and for each  $\omega$ . In figure 19, approximation of the curvature field  $\kappa'_3$  obtained on the grid  $m_3$  with  $\epsilon_h = \Delta x/2$  is presented.

For each grid  $m_i$  the  $\mathbf{x}_i^\omega$  and  $\mathbf{x}_i^{\omega, \kappa'}$  iso-lines are divided into  $N_i^s$  sample points; hence, the error of the interface curvature approximation is defined as

$$L_{1,i}^\kappa = \frac{1}{N_i^s} \sum_{l=1}^{N_i^s} |\mathbf{r}_{i,l}^{\kappa'} - \mathbf{r}_{i,l}^\Gamma|, \quad (39)$$

where  $\mathbf{r}_{i,l}^{\kappa'} = |\mathbf{x}_{i,l}^{\omega, \kappa'} - \mathbf{x}_0|$  and  $\mathbf{r}_{i,l}^\Gamma = |\mathbf{x}_{i,l}^\omega - \mathbf{x}_0|$ ,  $\mathbf{x}_0$  is the center of the circular

interface. Such formula for the error accounts only for the error in the curvature approximation  $\kappa'_i$ , and distinguishes it from the error in the interface  $\Gamma$  position approximation.

In tables 1 and 2, results of the curvature  $\kappa'_i$  convergence study on five grids  $m_i$  and after  $N_\tau = 256$  re-initialization steps are given, for the two interface widths  $\epsilon_h = \Delta x/2$  and  $\epsilon_h = \Delta x\sqrt{2}/4$ , respectively.

m.f.	$\psi_1(\alpha, \gamma_1)$		$\psi_1(\alpha, \gamma_2)$		$\psi_0(\mathbf{x}, t)$	
$\Gamma$	$\alpha$	$\psi'_0(\psi_1)$	$\alpha$	$\psi'_0(\psi_1)$	$\alpha$	$\psi_0(\alpha)$
$m_1$	4.5127e-3	3.7965e-3	4.0082e-3	2.9365e-3	4.0082e-3	2.9365e-3
$m_2$	1.8758e-3	6.9689e-4	1.9332e-3	2.1592e-4	1.9333e-3	2.1591e-4
$m_3$	9.6959e-4	7.2554e-4	8.9694e-4	1.4100e-4	8.9634e-4	1.4258e-4
$m_4$	8.1422e-4	8.0377e-4	2.6027e-4	4.1669e-5	2.6027e-4	4.1669e-5
$m_5$	3.2637e-2	3.2472e-2	1.4827e-4	1.0275e-5	1.4827e-4	1.0275e-5
$m_1$	5.3185e-3	5.2789e-3	4.9513e-3	4.9016e-3	4.9513e-3	4.9016e-3
$m_2$	5.0811e-4	5.8833e-4	3.0678e-4	1.5043e-4	3.0676e-4	1.5044e-4
$m_3$	5.2778e-4	5.8279e-4	1.9617e-4	1.3111e-4	1.9617e-4	1.3111e-4
$m_4$	7.7801e-4	7.3043e-4	1.0271e-4	3.7678e-5	1.0271e-4	3.7678e-5
$m_5$	2.9551e-2	2.9521e-2	4.0428e-5	1.0021e-5	4.0428e-5	1.0021e-5
$m_1$	5.9374e-3	6.3264e-3	5.5758e-3	5.8275e-3	5.5758e-3	5.8275e-3
$m_2$	1.7941e-3	8.8314e-4	1.2051e-3	1.3091e-4	1.2051e-3	1.3091e-4
$m_3$	1.1891e-3	7.3411e-4	6.6088e-4	1.0361e-4	6.6330e-4	1.0460e-4
$m_4$	1.0401e-3	7.8492e-4	4.6755e-4	3.6848e-5	4.6755e-4	3.6848e-5
$m_5$	2.6359e-2	2.6527e-2	2.3224e-4	9.6314e-6	2.3224e-4	9.6314e-6

Table 1: Convergence of the curvature  $\kappa'_i$  at  $\alpha(\mathbf{x}, t) = (0.05, 0.5, 0.95)$  iso-lines (from top to bottom) after  $N_\tau = 256$  re-initialization steps, the interface width  $\epsilon_h = \Delta x/2$ . Errors are defined using  $L_{1,i}^\kappa$  norm given by Eq. (39). The results are calculated on five grids  $m_i$  with three mapping functions (m.f.)  $\psi_1(\alpha, \gamma_1)$ ,  $\psi_1(\alpha, \gamma_2)$ ,  $\psi_0(\mathbf{x}, t)$  and two interface representations  $\Gamma(\alpha(\psi_0))$  and  $\Gamma(\psi_0(\alpha) \approx \psi'_0(\psi_1))$ .

In tables 3 and 4, the errors from tables 1-2 averaged in the narrow band  $(0.05, 0.5, 0.95)$  are presented. The results in tables 3 and 4 are depicted in

m.f.	$\psi_1(\alpha, \gamma_1)$		$\psi_1(\alpha, \gamma_2)$		$\psi_0(\mathbf{x}, t)$	
$\Gamma$	$\alpha$	$\psi'_0(\psi_1)$	$\alpha$	$\psi'_0(\psi_1)$	$\alpha$	$\psi_0(\alpha)$
$m_1$	3.3388e-3	2.2473e-3	3.7087e-3	4.0166e-4	3.7087e-3	4.0166e-4
$m_2$	1.7094e-3	1.2542e-3	2.5111e-3	5.2983e-4	2.5111e-3	5.2979e-4
$m_3$	1.5087e-3	1.7981e-3	1.2191e-3	1.6811e-4	1.2191e-3	1.6811e-4
$m_4$	2.3557e-3	2.4407e-3	3.9579e-4	4.0151e-5	3.9579e-4	4.0151e-5
$m_5$	3.1094e-3	3.0644e-3	1.8679e-4	1.0546e-5	1.8679e-4	1.0546e-5
$m_1$	3.5091e-3	2.6268e-3	2.3302e-3	1.4589e-3	2.3302e-3	1.4589e-3
$m_2$	8.0637e-4	1.0710e-3	7.4319e-4	3.5706e-4	7.4319e-4	3.5708e-4
$m_3$	1.4803e-3	1.6132e-3	3.2301e-4	1.4815e-4	3.2301e-4	1.4815e-4
$m_4$	2.8712e-3	2.6359e-3	1.8123e-4	3.8763e-5	1.8123e-4	3.8763e-5
$m_5$	2.5595e-3	2.5462e-3	7.2441e-5	1.0676e-5	7.2441e-5	1.0676e-5
$m_1$	6.8061e-3	3.8563e-3	5.4077e-3	2.9623e-3	5.4077e-3	2.9623e-3
$m_2$	2.6807e-3	1.3214e-3	1.7051e-3	2.7312e-4	1.7051e-3	2.7313e-4
$m_3$	1.8291e-3	1.5433e-3	7.0173e-4	1.3536e-4	7.0173e-4	1.3536e-4
$m_4$	2.5678e-3	2.3315e-3	6.8413e-4	3.7086e-5	6.8413e-4	3.7086e-5
$m_5$	3.0363e-3	2.8712e-3	3.1737e-4	1.0543e-5	3.1737e-4	1.0543e-5

Table 2: Convergence of the curvature  $\kappa'_i$  at  $\alpha(\mathbf{x}, t) = (0.05, 0.5, 0.95)$  iso-lines (from top to bottom) after  $N_\tau = 256$  re-initialization steps, the interface width  $\epsilon_h = \Delta x \sqrt{2}/4$ . Errors are defined using  $L^{\kappa}_{1,i}$  norm given by Eq. (39). The results are calculated on five grids  $m_i$  with three mapping functions (m.f.)  $\psi_1(\alpha, \gamma_1)$ ,  $\psi_1(\alpha, \gamma_2)$ ,  $\psi_0(\mathbf{x}, t)$  and two interface representations  $\Gamma(\alpha(\psi_0))$  and  $\Gamma(\psi_0(\alpha) \approx \psi'_0(\psi_1))$ .

Fig. 21, and they can be interpreted as the convergence rate of the circular interface curvature in the narrow band  $0.05 \leq \alpha(\mathbf{x}, t) \leq 0.95$  with two different  $\delta(\alpha)/\epsilon_h$  support widths  $\epsilon_h = \Delta x/2$  or  $\epsilon_h = \Delta x \sqrt{2}/4$ .

In figure 21, one observes that the second order convergence rate of the curvature is achieved for the mapping functions  $\psi_1(\alpha, \gamma_2)$  and  $\psi_0(\alpha)$  when the signed distance function interface representations given by  $\psi_0(\alpha) \approx \psi'_0(\psi_1(\alpha, \gamma_2))$  are chosen. The convergence rates of the interface curvature differ dependent on whether the interface is represented by  $\alpha(\psi_0)$  or  $\psi_0(\alpha)$ . This latter observa-

m.f.	$\psi_1(\alpha, \gamma_1)$		$\psi_1(\alpha, \gamma_2)$		$\psi_0(\mathbf{x}, t)$	
$\Gamma$	$\alpha$	$\psi'_0(\psi_1)$	$\alpha$	$\psi'_0(\psi_1)$	$\alpha$	$\psi_0$
$m_1$	5.2562e-3	5.1339e-3	4.8451e-3	4.5552e-3	4.8451e-3	4.5552e-3
$m_2$	1.3927e-3	7.2278e-4	1.1484e-3	1.6575e-4	1.1484e-3	1.6576e-4
$m_3$	8.9547e-4	6.8082e-4	5.8466e-4	1.2524e-4	5.8531e-4	1.2613e-4
$m_4$	8.7741e-4	7.7305e-4	2.7684e-4	3.8732e-5	2.7684e-4	3.8732e-5
$m_5$	2.9515e-2	2.9506e-2	1.4031e-4	9.9756e-6	1.4031e-4	9.9756e-6

Table 3: Convergence of the curvature  $\kappa'_i$  in the narrow band of  $0.05 \leq \alpha(\mathbf{x}_\Gamma, t) \leq 0.95$  the interface width  $\epsilon_h = \Delta x/2$ . The table contains arithmetical mean of the values in appropriate columns and rows of Tab. 1.

m.f.	$\psi_1(\alpha, \gamma_1)$		$\psi_1(\alpha, \gamma_2)$		$\psi_0(\mathbf{x}, t)$	
$\Gamma$	$\alpha$	$\psi'_0(\psi_1)$	$\alpha$	$\psi'_0(\psi_1)$	$\alpha$	$\psi_0$
$m_1$	4.5513e-3	2.9101e-3	3.8155e-3	1.6076e-3	3.8155e-3	1.6076e-3
$m_2$	1.7322e-3	1.2156e-3	1.6531e-3	3.8667e-4	1.6531e-3	3.8666e-4
$m_3$	1.6061e-3	1.6515e-3	7.4794e-4	1.5054e-4	7.4794e-4	1.5054e-4
$m_4$	2.5982e-3	2.4694e-3	4.2038e-4	3.8666e-5	4.2038e-4	3.8666e-5
$m_5$	2.9017e-3	2.8272e-3	1.9220e-4	1.0588e-5	1.9220e-4	1.0588e-5

Table 4: Convergence of the curvature  $\kappa'_i$  in the narrow band of  $0.05 \leq \alpha(\mathbf{x}_\Gamma, t) \leq 0.95$  the interface width  $\epsilon_h = \sqrt{2}\Delta x/4$ . The table contains arithmetical mean of the values in appropriate columns and rows of Tab. 2.

tion is explained by the fact that to reconstruct the jump at  $\Gamma$  the level-set function  $\alpha(\psi_0(\mathbf{x}, t))$  requires the constant number of grid points (from five to three dependent on selected  $\epsilon_h$ , see Fig. 7) regardless of the grid resolution used in simulation. At the same time, the accuracy of the representation of the signed distance function  $\psi_0(\alpha)$ , or its approximation  $\psi'_0(\psi_1(\alpha, \gamma_2))$ , increases proportionally to the number of grid points  $N_c$ .

In the case of the mapping function  $\psi_1(\alpha, \gamma_1)$ , convergence of the interface curvature is not achieved although equation (1) is solved to a fully convergent state on all grids  $m_i$ ,  $i = 1, \dots, 5$ , see Fig. 18. This result may be explained

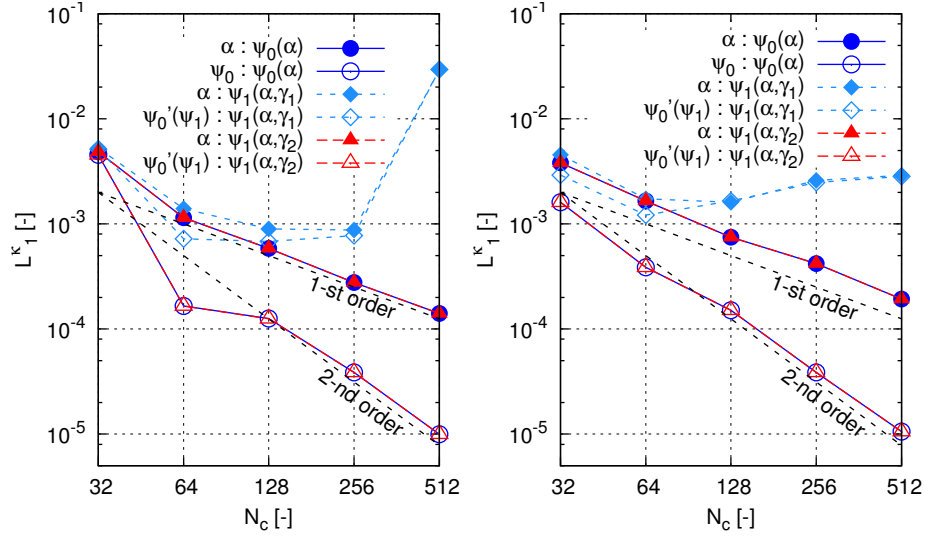


Figure 21: Convergence of the 2D circular interface curvature  $\kappa'_i$  in the narrow band of the level-set function  $0.05 \leq \alpha(\mathbf{x}, t) \leq 0.95$  with (a)  $\epsilon_h = \Delta x/2$  and (b)  $\epsilon_h = \Delta x\sqrt{2}/4$  after  $N_\tau = 256$  re-initialization steps. In the legend  $\alpha : \psi_0(\alpha)$ , the symbol on the left denotes the interface representation, the symbol on the right denotes the mapping function used to compute derivatives in Eq. (35).  $N_c$  is the number of grid points in  $x, y$  directions.

by the existence of a non-zero second order derivative of  $\psi_1(\alpha, \gamma_1)$  function from the interface  $\mathbf{x}_\Gamma$  that impairs the calculation of the interface curvature, see Fig. 11(b).

For both interface widths  $\epsilon_h = \Delta x/2$  or  $\epsilon_h = \sqrt{2}\Delta x/4$ , the second order convergence rate of  $\kappa'_i$  is obtained for  $\psi_0(\alpha)$  and  $\psi_1(\alpha, \gamma_2)$ , see Fig. 21. This confirms discussion regarding the allowable width of the  $\delta(\alpha)/\epsilon_h$  support presented in Section 5.2. The two-three grid points (see Fig. 7 and Fig. 14) required to reconstruct the interface curvature  $\kappa$  with second-order accuracy are also needed in the construction of the flux limiters during a solution of the advection equation (34); the two-three grid points is a typical resolution of the VOF interface capturing methods [19, 20, 21, 22].

### 6.1.3. Wavy interface

McCaslin and Desjardins [16] noticed the feedback mechanism between erroneous normals  $\mathbf{n}_\Gamma$  and the solution of the re-initialization equation (1) when  $N_\tau \gg 1$ . This numerical phenomenon occurs due to errors introduced during discretization of equation (1) and leads to artificial deformations of the level-set function  $\alpha(\psi_0(\mathbf{x}, t))$  increasing with time  $\tau$ . According to [16], this defect in the re-initialization procedure is particularly noticeable in regions where the interface  $\Gamma$  is stationary. In order to reduce this erroneous feedback between  $\mathbf{n}_\Gamma$  and  $\alpha(\psi_0(\mathbf{x}, t))$  in [16] it is proposed to vary the amount of re-initialization spatially and to localize the solution of Eq. (1) only in the regions where the interface is advected or  $|\mathbf{n}_\Gamma \cdot \mathbf{u}| \gg 1$ . With this method, an additional function  $\beta(\mathbf{x}, t)$ , variable in time and space is introduced. The diffusive and compressive fluxes on the RHS of equation (1) are multiplied by  $\beta(\mathbf{x}, t)$  to localize re-initialization depending on the local flow conditions. The function  $\beta(\mathbf{x}, t)$  has to satisfy the condition  $\mathbf{n}_\Gamma \cdot \nabla\beta = 0$  used to introduce an additional equation for  $\beta(\mathbf{x}, t)$ . We recognize that in the method put forward by the present paper  $\delta(\alpha)$  given by Eq. (25) (see also Eqs. (32) and (33)), plays a role similar to the function  $\beta(\mathbf{x}, t)$  in [16]. However, in the present work, we do not need to vary the number of re-initialization steps in time and space relative to local flow conditions.

In this section, we carry out re-initialization of the 3D wavy interface similar to the test case proposed in [16]. The initial condition to Eq. (1) is given by Eq. (2) where the signed distance function

$$\psi_0(\mathbf{x}, t) = 1/2 - y + A_0 \sin(4\pi x) \sin(4\pi z), \quad (40)$$

defines the wavy interface,  $A_0 = 0.03125 m$  on all grids  $m_i$ . Substitution of Eq. (40) into Eq. (2) allows us to compute the exact curvature  $\kappa$  of the interface  $\Gamma$ . Convergence of  $\kappa'_i$ , which is a numerical approximation of the exact interface curvature  $\kappa_i$ , is studied on the four gradually refined meshes:  $m_i = 2^{4+i} \times 2^{4+i} \times 2^{4+i}$  where  $i = 2, \dots, 4$  and a mesh  $m_{3.5} = 192 \times 192 \times 192$  with the number of grid nodes in-between  $m_3, m_4$ . The computational domain is a cubic box  $\Omega = \langle -0.5, 0.5 \rangle \times \langle 0, 1 \rangle \times \langle -0.5, 0.5 \rangle m^3$  discretized using a uniform

grid nodes distribution, the time step size is set to  $\Delta\tau = D/C^2 = \epsilon_h$ .

Using experience gained in the previous 2D test cases (see Sec. 6.1.2), two mapping functions  $\psi_0(\alpha)$  and  $\psi_1(\alpha, \gamma_2)$  are used for discretization of  $|\nabla\alpha|$  in Eq. (1). Similar to the previous example, we focus on convergence of the interface curvature in the narrow band  $0.05 \leq \alpha \leq 0.95$ . Additionally, as in Section 6.2, the influence of the  $\delta(\alpha)/\epsilon_h$  support width  $\epsilon_h = \Delta x/2$  or  $\epsilon_h = \sqrt{3}\Delta x/4$  on convergence rate of  $\kappa'_i$  is studied. To assess effects of the  $\alpha - \mathbf{n}_\Gamma$  coupling on the interface deformations, we consider three test cases in which  $\mathbf{n}_\Gamma$  is constant or variable in time  $\tau$ :

$T_1$  :  $\mathbf{n}_\Gamma = \text{const}$ ,  $\nabla\alpha$  is calculated before first iteration,  $N_\tau = 1024$ ,  $\epsilon_h = \Delta x/2$ .

$T_2$  :  $\mathbf{n}_\Gamma \neq \text{const}$ ,  $\nabla\alpha$  is calculated before each iteration,  $N_\tau = 1024$ ,  $\epsilon_h = \Delta x/2$ .

$T_3$  : as the case  $T_2$  but with  $\epsilon_h = \sqrt{3}\Delta x/4$ .

*Computation of numerical errors in the wavy interface curvature.* In the beginning, we note that the curvature  $\kappa$  derived from the analytical solution given by Eq. (2) and Eq. (40) is exact only at the interface  $\Gamma$ . The comparison with  $\kappa'$  that is calculated away from the interface  $\Gamma$  may lead to incorrect interpretations of the convergence results in the narrow band of the level-set function  $0.05 \leq \alpha \leq 0.95$ . This is due to the 3D wavy interface curvature  $\kappa_i \neq \text{const}$ , in the direction normal and tangential to the interface  $\Gamma$ . For this reason, computation of the errors in the numerical approximation  $\kappa'_i$  of the exact curvature  $\kappa_i$ , is performed two ways. In the first approach, the error of the numerical solution is determined directly from the difference between  $\kappa_i$  and  $\kappa'_i$ , which are both computed in the centers of the control volumes  $N_i^p$  localized in the narrow band  $0.05 \leq \alpha \leq 0.95$  on the mesh  $m_i$ . The  $L_1^\kappa$ ,  $L_2^\kappa$  and  $L_\infty^\kappa$  norms on the mesh  $m_i$  are defined by following formulas

$$L_{1,i}^\kappa = \frac{1}{N_i^p} \sum_{l=1}^{N_i^p} |\kappa_l - \kappa'_l|, \quad (41)$$

$$L_{2,i}^\kappa = \frac{1}{N_i^p} \left[ \sum_{l=1}^{N_i^p} (\kappa_l - \kappa'_l)^2 \right]^{1/2}, \quad (42)$$

$$L_{\infty,i}^\kappa = \max(|\kappa_l - \kappa'_l|), \quad l = 1, \dots, N_i^p. \quad (43)$$

In the second approach, the convergence rate of  $\kappa'_i$  is determined dependent on the interface representation: by the conservative level-set function  $\Gamma(\alpha(\mathbf{x}_i, t))$  or by the signed distance function  $\Gamma(\psi_0(\alpha))$ . Since in the present case the curvature  $\kappa_i$  is variable in space and the relation between  $\kappa'_i$  and  $\mathbf{x}_{i,\Gamma}$  is not known, it is very difficult to apply the procedure presented in Section 6.1.2 for computation of  $\kappa'_i$ . For this reason, we use a simplified approach using available post-processing tools. First, we calculate  $\kappa_i$  and  $\kappa'_i$  in the centers of the control volumes, then the norm  $L_i^\kappa = \kappa_i - \kappa'_i$  is evaluated. Afterwards,  $L_i^\kappa$  is interpolated to the interface represented by the conservative level-set function  $\Gamma(\alpha(\mathbf{x}_i, t))$  or the signed distance function  $\Gamma(\psi_0(\alpha))$  obtained as iso-surfaces in the post-processing software. The maximal value of  $|L_i^\kappa(\Gamma(\alpha))|$  or  $|L_i^\kappa(\Gamma(\psi_0))|$  on grid  $m_i$  allows us to estimate  $L_{\infty,i}^\kappa(\alpha)$  and  $L_{\infty,i}^\kappa(\psi_0)$  norms at  $\Gamma(\alpha)$  and  $\Gamma(\psi_0)$ , respectively.

*Convergence of the re-initialization equation.* In figure 22 convergence of the solution to Eq. (1) in the test cases  $T_1$ ,  $T_2$  and  $T_3$  with two mapping functions  $\psi_0(\alpha)$  and  $\psi_1(\alpha, \gamma_2)$  is presented. We observe that to obtain the stationary solution (the constant convergence level) about  $N_\tau \approx 100$  iterations are needed in the cases  $T_1$ ,  $T_2$  and about  $N_\tau \approx 200$  iterations in the test case  $T_3$  (here only  $\psi_0(\alpha)$  is used).

We note that at least second-order convergence rate of  $L_1$  norm (defined by Eq. (9)) in time  $\tau$  may be deduced from Fig. 22 in the all three test cases. Surprisingly, the rate of convergence of the solution to Eq. (1) is exactly the same in the test cases  $T_1$  and  $T_2$ , see Fig. 22(a)(b). Since the interface curvature  $\kappa$  is implicitly included in the re-initialization equation (1) (see Eqs. (32) and (33)), previously discussed numerical errors introduced by calculation of gradients in

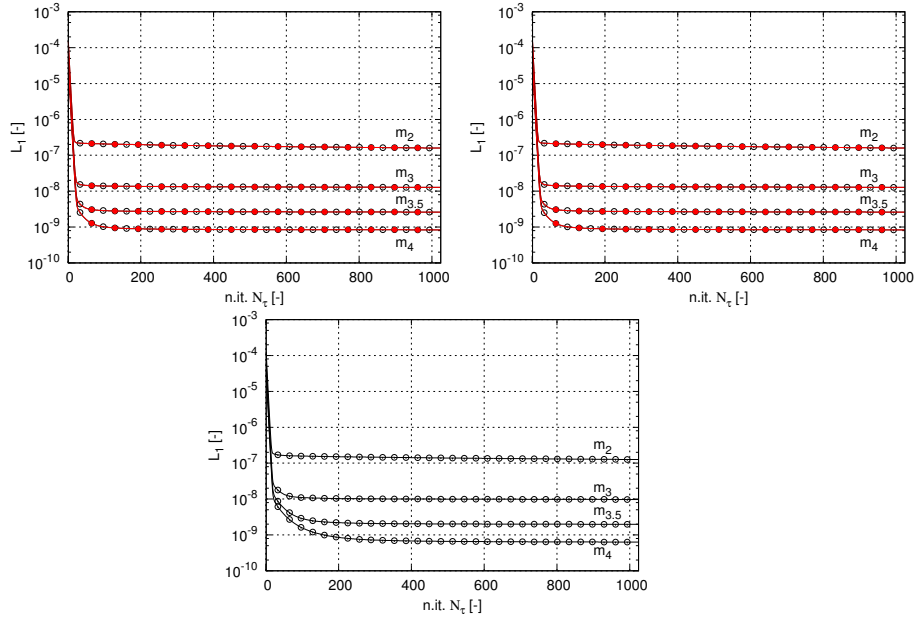


Figure 22: Convergence of the solution to re-initialization Eq. (1) in the test cases (a)  $T_1$ , (b)  $T_2$ , (c)  $T_3$ .  $|\nabla\alpha|$  is discretized using the mapping functions  $\psi_0(\alpha)$  (black void dots)  $\psi'_0(\psi_1(\alpha, \gamma_2))$  (red solid dots), the results were obtained on four gradually refined grids  $m_i$ ,  $L_1$  norm is defined by Eq. (9).

2D-3D space have a larger impact on the convergence rate than the errors in computation of  $\kappa$ .

The convergence rate in the test case  $T_3$  presented in Fig. 22(c) is lower than in previously discussed tests  $T_1, T_2$ . This result is to some degree in opposition to the convergence studies presented in figures 6 and 18. However, the wavy interface curvature is variable not only in the direction normal but also in the direction tangential to the interface  $\Gamma$ . For this reason the reduced number of grid points when the interface width is set to  $\epsilon_h = \sqrt{3}\Delta x/4 < \Delta x/2$  may lead to slower convergence.

*Errors in computations of the wavy interface curvature.* During numerical experiment  $T_1$  it was found that values of the errors defined by equations (41)-(43) remain constant and equal to error after  $N_\tau = 1$  re-initialization steps, see table

5. Similar to the convergence rates presented in Fig. 22, the values of the norms defined by Eqs. (41) and (43) in table 5 are identical for the mapping functions  $\psi_1(\alpha, \gamma_2)$  and  $\psi_0(\alpha)$ . This result is consistent with data presented in tables 1-2 and is expected in the light of equation (20).

m.f.	$\psi_1(\alpha, \gamma_2)$			$\psi_0(\alpha)$		
	$L_1^\kappa$	$L_2^\kappa$	$L_\infty^\kappa$	$L_1^\kappa$	$L_2^\kappa$	$L_\infty^\kappa$
$m_2$	4.6636e-2	5.7389e-2	1.2425e-1	4.6636e-2	5.7389e-2	1.2425e-1
$m_3$	1.1639e-2	1.4403e-2	3.1545e-2	1.1639e-2	1.4403e-2	3.1545e-2
$m_{3.5}$	5.1776e-3	6.4156e-3	1.4061e-2	5.1776e-3	6.4156e-3	1.4061e-2
$m_4$	2.9106e-3	3.6092e-3	7.9169e-3	2.9106e-3	3.6092e-3	7.9169e-3

Table 5: The  $L_1^\kappa$ ,  $L_2^\kappa$  and  $L_\infty^\kappa$  norms obtained using Eqs. (41) and (43) in the test case  $T_1$  after  $N_\tau = 1024$  re-initialization steps.

m.f.	$\psi_0(\alpha)$		
	$L_1^\kappa$	$L_2^\kappa$	$L_\infty^\kappa$
$m_2$	4.6414e-2	5.7396e-2	1.2425e-1
$m_3$	1.1657e-2	1.4478e-2	3.1545e-2
$m_{3.5}$	5.2041e-3	6.4583e-3	1.4060e-2
$m_4$	2.9263e-3	3.6317e-3	7.9169e-3

Table 6: The  $L_1^\kappa$ ,  $L_2^\kappa$  and  $L_\infty^\kappa$  norms obtained using Eqs. (41) and (43) in the test case  $T_3$  after  $N_\tau = 1$  re-initialization steps.

In figure 23, the evolution of the errors recorded during test cases  $T_1$ ,  $T_2$  and  $T_3$  are depicted. We note that after the first re-initialization step, levels of the all errors are equal to the values obtained in the test case  $T_1$  (compare results in Fig. 23 at  $N_\tau = 1$  with values in tables 5-6). When  $N_\tau > 1$  values of the errors grow, but after about  $N_\tau \approx 6$  iterations they reach an almost constant level which remain until the end of re-initialization. Such behavior is observed in the three finest meshes  $m_2$ ,  $m_{3.5}$ ,  $m_4$ . The solution in the mesh  $m_2$  is somewhat unresolved, since in this case we have only two grid nodes per wave amplitude

(in [16] three nodes were used). The end values of the errors obtained in the

m.f.	$\psi_1(\alpha, \gamma_2)$			$\psi_0(\alpha)$		
L	$L_1^\kappa$	$L_2^\kappa$	$L_\infty^\kappa$	$L_1^\kappa$	$L_2^\kappa$	$L_\infty^\kappa$
$m_2$	2.7461e-1	3.5492e-1	1.51936	2.7461e-1	3.5492e-1	1.51936
$m_3$	1.0791e-1	1.4944e-1	6.2188e-1	1.0791e-1	1.4944e-1	6.2188e-1
$m_{3.5}$	6.8839e-2	9.7209e-2	3.8353e-1	6.8839e-2	9.7209e-2	3.8353e-1
$m_4$	5.0941e-2	7.2103e-2	2.7458e-1	5.0941e-2	7.2103e-2	2.7458e-1

Table 7: The  $L_1^\kappa$ ,  $L_2^\kappa$  and  $L_\infty^\kappa$  norms obtained using Eqs. (41) and (43) in the test case  $T_2$  after  $N_\tau = 1024$  re-initialization steps.

m.f.	$\psi_0(\alpha)$		
L	$L_1^\kappa$	$L_2^\kappa$	$L_\infty^\kappa$
$m_2$	2.4721e-1	3.2123e-1	1.210778
$m_3$	1.0624e-1	1.4785e-1	5.8091e-1
$m_{3.5}$	6.8784e-2	9.7189e-2	3.7048e-1
$m_4$	5.1173e-2	7.2384e-2	2.6857e-1

Table 8: The  $L_1^\kappa$ ,  $L_2^\kappa$  and  $L_\infty^\kappa$  norms obtained using Eqs. (41) and (43) in the test case  $T_3$  after  $N_\tau = 1024$  re-initialization steps.

test cases  $T_2$ ,  $T_3$  are given in tables 7-8, respectively.

In figure 24, the results given in tables 5-8 are depicted. We observe that at  $N_\tau = 1$  (and in the test case  $T_1$ ) errors defined by equations (41)-(43) show the second order convergence rate. We emphasize once again that in the test case  $T_1$ , the values of all errors remain constant during all  $N_\tau = 1024$  steps. Hence, for  $\mathbf{n}_\Gamma = \text{const}$  in time  $\tau$  the second-order convergence rate is also achieved in the narrow band of  $\alpha(\psi_0)$ . In the test cases  $T_2$  and  $T_3$ , the first-order convergence rate of the interface curvature is detected in the narrow band of the conservative level set function  $0.05 \leq \alpha(\psi_0) \leq 0.95$ .

As discussed previously, there is yet another way in which the errors in  $\kappa'$  may be estimated. In tables 9-10, values of the  $L_\infty^\kappa = \max(|L^\kappa| = |\kappa - \kappa'|)$  norms

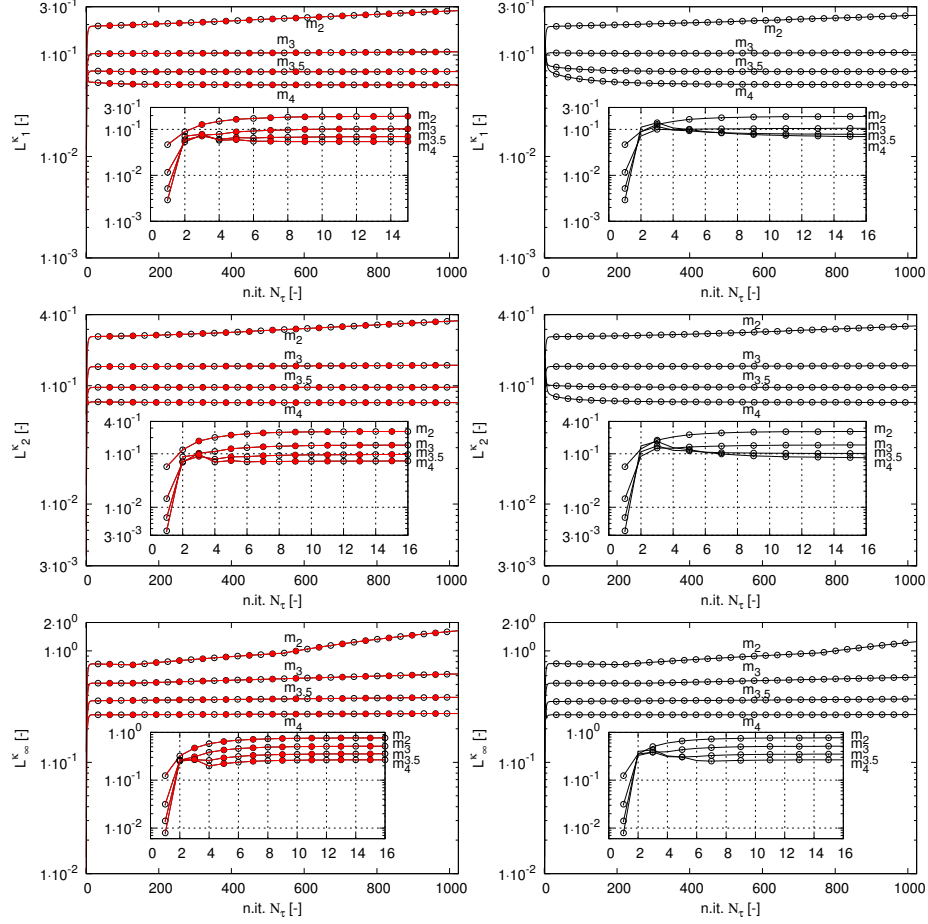


Figure 23: Convergence of  $L_1^\kappa$ ,  $L_2^\kappa$  and  $L_\infty^\kappa$  norms during  $N_\tau = 1024$  re-initialization steps of the 3D wavy interface with Eq. (1) in the test cases:  $T_2$  (left) and  $T_3$  (right).  $|\nabla\alpha|$  is discretized using mapping functions  $\psi_0(\alpha)$  (black void dots) and  $\psi'_0(\psi_1(\alpha, \gamma_2))$  (red solid dots).

obtained with the mapping functions  $\psi_1(\alpha, \gamma_2)$ ,  $\psi_0(\alpha)$  in the test cases  $T_2$ ,  $T_3$  are given. Here, almost no difference is detected between the convergence rates obtained using  $\Gamma(\alpha(\psi_0))$  or  $\Gamma(\psi_0(\alpha))$  interface representations, also depicted in figure 24(c)(f). The values in tables 9-10 show the second-order convergence rate of  $\kappa'_i$  is detected if we take into account only the errors at the interface  $\Gamma(\alpha)$  or  $\Gamma(\psi_0)$  (compare with  $L_\infty^\kappa$  norms presented in figures 25-27). In the case  $T_3$ ,

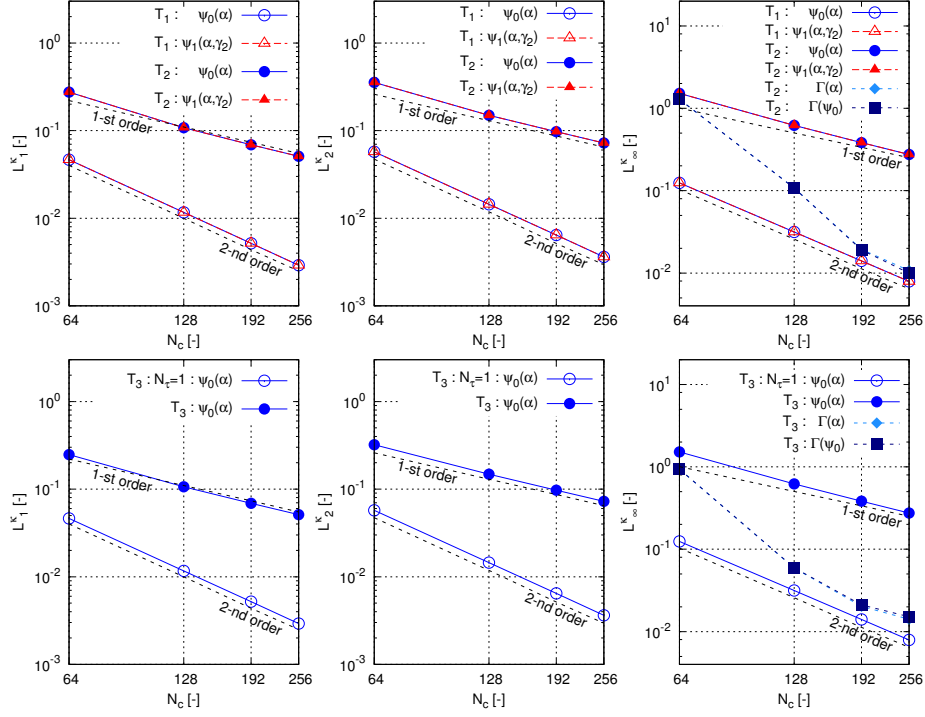


Figure 24: The comparison of convergence rates for  $L_1^\kappa$ ,  $L_2^\kappa$  and  $L_\infty^\kappa$  norms after  $N_\tau = 1$  (void symbols) and  $N_\tau = 1024$  (solid symbols) re-initialization steps in the test cases  $T_1$ ,  $T_2$  (top) and  $T_3$  (bottom).  $|\nabla\alpha|$  in Eq. (1) is discretized using the mapping functions  $\psi_0(\alpha)$  (dots, diamonds, squares) and  $\psi'_0(\psi_1(\alpha, \gamma_2))$  (triangles).

the convergence rate of  $\kappa'_i$  on the finest grid  $m_4$  is somewhat lower; this may be explained by the reduced number of grid points due to the smaller interface width  $\epsilon_h = \sqrt{3}\Delta x/4 < \Delta x/2$  used to resolve  $\alpha(\psi_0)$  and  $\psi_0(\alpha)$ .

Finally, in figures 25-27 we can compare shapes of the reconstructed interfaces obtained in the test cases  $T_i$  where  $i = 1, 2, 3$ . The differences in the interface  $\Gamma$  shapes presented in these figures are barely recognizable. The shape of the wavy interface is preserved on all meshes used in the present study almost independently from the number of re-initialization steps  $N_\tau$ . Although the reduction of the interface width  $\epsilon_h$  leads to slower convergence of the solution to the re-initialization equation, and slower convergence of its curvature  $\kappa'_i$ ,

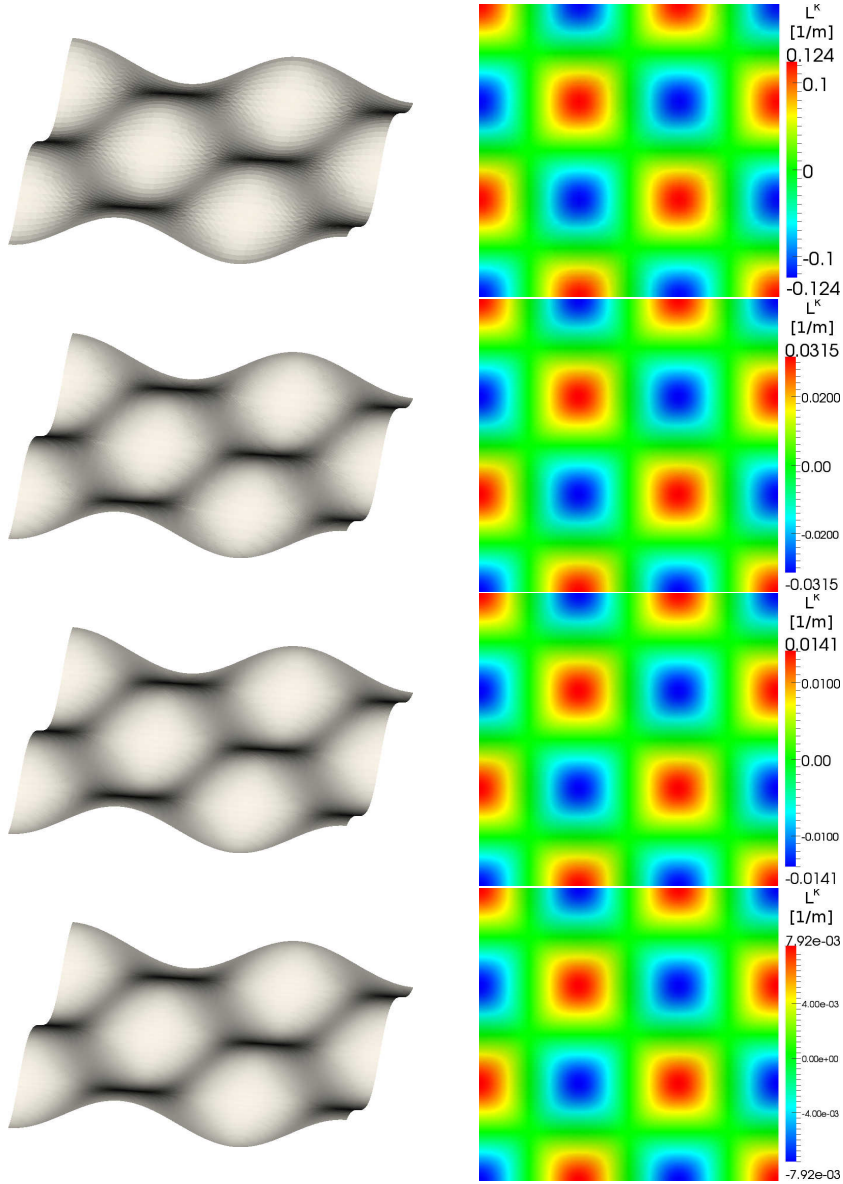


Figure 25: The comparison of  $\Gamma(\psi_0)$  (left) and  $L_i^k = \kappa_i - \kappa'_i$  norms (right) in the test case  $T_1$  on four grids  $m_1, m_2, m_{3.5}$  and  $m_4$  from top to bottom. Re-initialization of the 3D wavy interface is performed with the mapping function  $\psi_0(\alpha)$ . The error  $L_i^k$  is interpolated to the interface  $\Gamma(\psi_0)$ , the interface width is set to  $\epsilon_h = \Delta x/2$ .

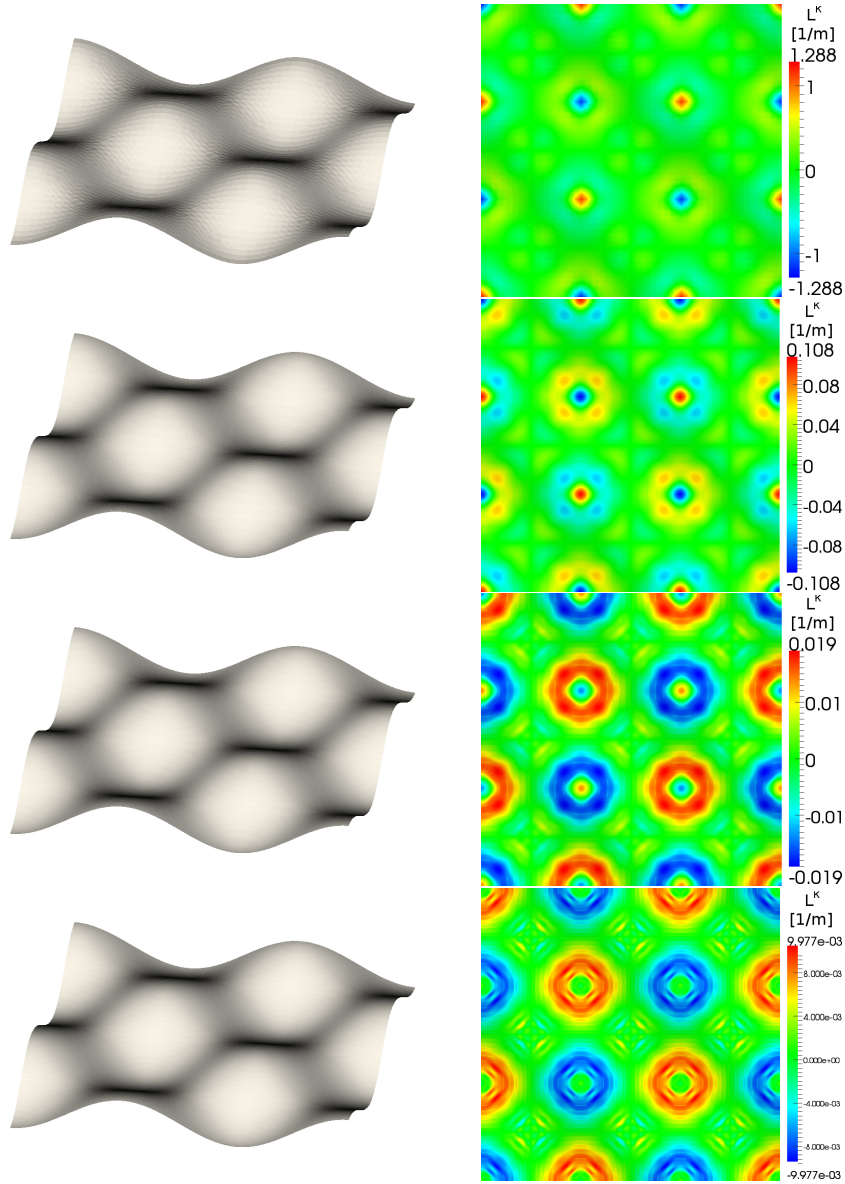


Figure 26: The comparison of  $\Gamma(\psi_0)$  (left) and  $L_i^\kappa = \kappa_i - \kappa'_i$  norms (right) in the test case  $T_2$  on four grids  $m_1$ ,  $m_2$ ,  $m_{3.5}$  and  $m_4$  from top to bottom. Re-initialization of the 3D wavy interface is performed with the mapping function  $\psi_0(\alpha)$ . The error  $L_i^\kappa$  is interpolated to the interface  $\Gamma(\psi_0)$ , the interface width is set to  $\epsilon_h = \Delta x/2$

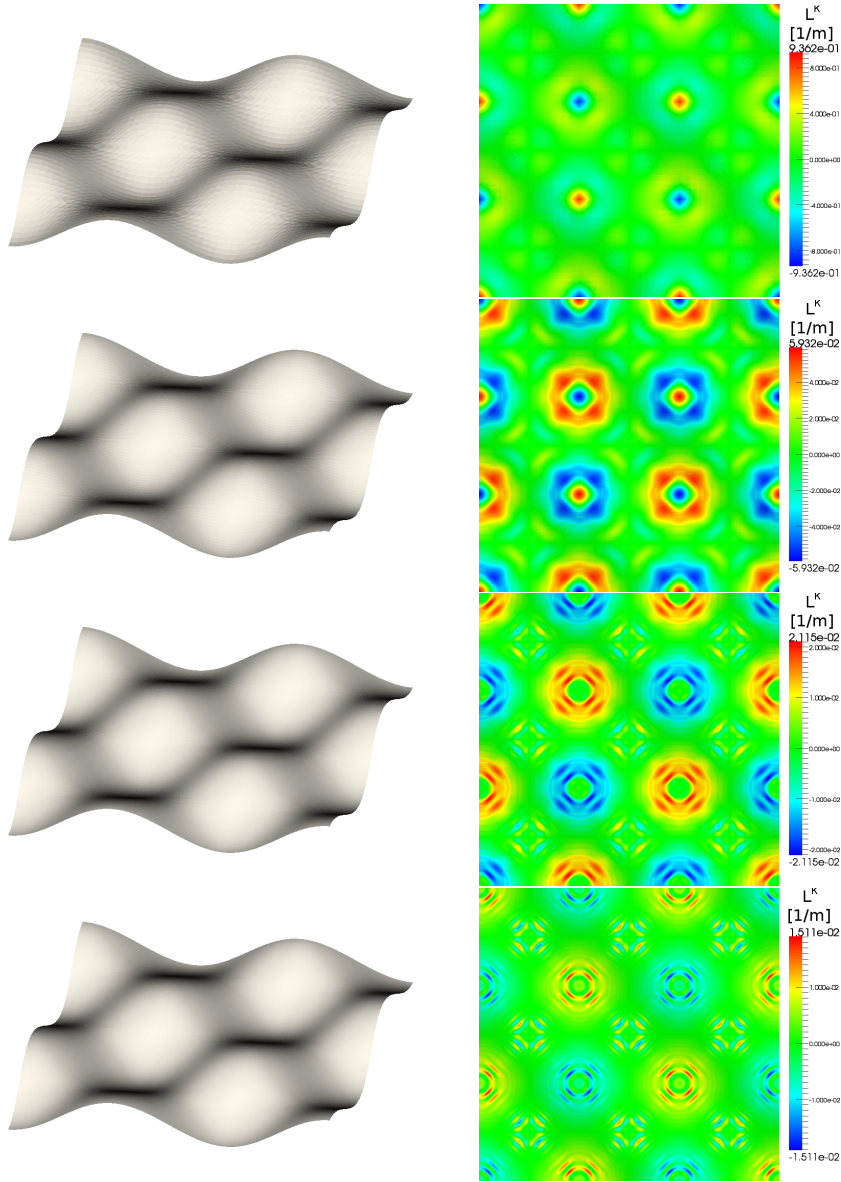


Figure 27: The comparison of  $\Gamma(\psi_0)$  (left) and  $L_i^\kappa = \kappa_i - \kappa'_i$  norms (right) in the test case  $T_3$  on four grids  $m_1$ ,  $m_2$ ,  $m_{3.5}$  and  $m_4$  from top to bottom. Re-initialization of the 3D wavy interface is performed with the mapping function  $\psi_0(\alpha)$ . The error  $L_i^\kappa$  is interpolated to the interface  $\Gamma(\psi_0)$ , the interface width is set to  $\epsilon_h = \sqrt{3}\Delta x/4$ .

m.f.	$\psi_1(\alpha, \gamma_2)$		$\psi_0(\alpha)$	
$\Gamma$	$\alpha$	$\psi'_0(\psi_1)$	$\alpha$	$\psi_0$
$m_2$	1.28881	1.28783	1.28763	1.28772
$m_3$	1.0813e-1	1.0771e-1	1.0816e-1	1.0767e-1
$m_{3.5}$	1.9419e-2	1.9067e-2	1.9413e-2	1.9061e-2
$m_4$	1.0741e-2	9.9776e-3	1.0721e-2	9.9771e-3

Table 9: Convergence of the interface curvature  $\kappa'_i$  measured by  $L^\infty$  norm obtained from  $|L_i^\kappa| = |\kappa_i - \kappa'_i|$  at the interface  $\Gamma(\alpha)$  and  $\Gamma(\psi_0)$  in the test case  $T_2$ , see figure 24(top).

m.f.	$\psi_0(\alpha)$	
$\Gamma$	$\alpha$	$\psi_0$
$m_2$	9.3597e-1	9.3625e-1
$m_3$	5.9071e-1	5.9321e-2
$m_{3.5}$	2.0281e-2	2.1154e-2
$m_4$	1.4133e-2	1.5113e-2

Table 10: Convergence of the curvature  $\kappa'_i$  obtained with the mapping function (m.f.)  $\psi_0(\alpha)$  measured by  $L^\infty$  norm obtained from  $|L_i^\kappa| = |\kappa_i - \kappa'_i|$  at the interface  $\Gamma(\alpha)$  and  $\Gamma(\psi_0)$  in the test case  $T_3$ , see figure 24(bottom).

this does not affect the wavy interface shape.

In summary, the results presented in tables 9-10 and in figure 24 confirm the second-order convergence rate of the interface curvature  $\kappa$  may be achieved within the second-order accurate finite volume solver using the conservative level-set method and the consistent re-initialization procedure.

## 6.2. Tests with advection

The primary aim of the studies performed below is verification of the new re-initialization method during advection of  $\alpha(\psi_0)$  and  $\psi_0(\alpha)$ . Next, we solve Eq. (34) with  $w_i = u_i$ , where  $u_i$  is the given divergence free velocity field. As we improve the re-initialization method first proposed in [1], similar advection test cases are carried out for comparison. In particular, we want to investigate the

area (mass) conservation of the new method in the case of the variable number of re-initialization steps  $N_\tau$ . Using experience gained during the tests in Section 6.1, only the mapping function  $\psi_0(\alpha)$  is used for discretization of  $|\nabla\alpha|$  in Eq. (1) and hence Eq. (32) is solved during the re-initialization step. The interface width is set to  $\epsilon_h = \sqrt{2}\Delta x/4$  and  $\Delta\tau = D/C^2 = \epsilon_h$ . Present investigations are performed in quadratic domain  $\Omega = \langle 0, 1 \rangle \times \langle 0, 1 \rangle \times m^2$  on gradually refined grids  $m_i = 2^{4+i} \times 2^{4+i}$  with the uniform grid nodes distribution.

The advection equation (34) is discretized in time using the first-order implicit Euler method, and in space using the deferred-correction method with the second-order TVD MUSCL flux limiter from [28]. This type of spatial and temporal discretization is a default technique used in the Fastest solver for discretization of advection terms in all transport equations. As the main goal of this paper is the improvement of the re-initialization method, the detailed solutions to numerical issues that arise during coupling of equations (32) and (34) are left for future investigations.

### 6.2.1. Rotating circle

In this section, a circular interface  $\Gamma$  revolving in the divergence free velocity field  $(u_1, u_2) = V_0/L(y - 0.5, 0.5 - x)$  where  $V_0 = 1 \text{ m/s}$  and  $L = 1 \text{ m}$  is studied. Initially at  $t = 0$ , the center of the circle with the radius  $R = 0.15 \text{ m}$  is located in the point  $(x_0, y_0) = (0.65 \text{ m}, 0.5 \text{ m})$ . The time step size during integration of equation (34) is set to  $\Delta t = 2\pi/N_t$ , where  $N_t = 360 \cdot i$  and  $i = 1, \dots, 4$  denotes the grid number.

In figure 28, convergence of the two interface representations  $\alpha(\psi_0)$  and  $\psi_0(\alpha)$  towards the initial condition is presented. As previously observed in [1], it is clear that an introduction of the re-initialization step after the advection step improves the conservation of the shape and area of the advected interface. In the previous sections we have shown that the new re-initialization method does not change the position of the stationary interfaces. For this reason small deformations of  $\Gamma$  after one revolution may be attributed to numerical errors introduced by the advection scheme, see Fig. 28. The main difference between

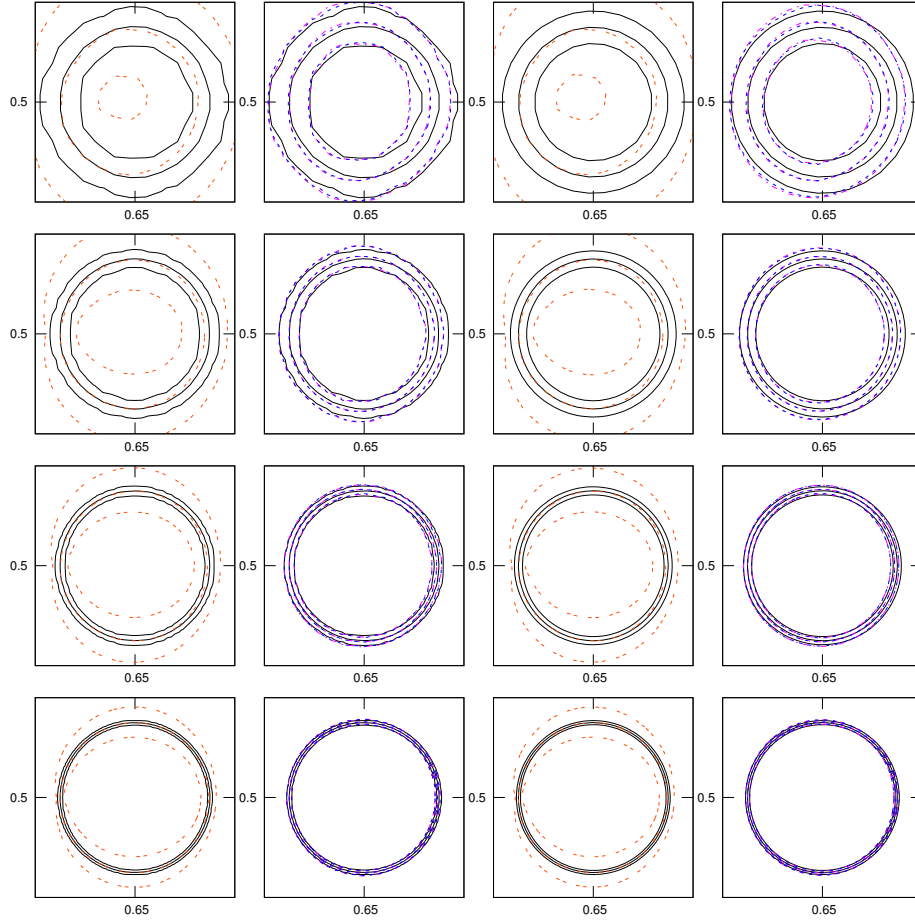


Figure 28: The comparison of  $\alpha(\psi_0) = (0.05, 0.5, 0.95)$  iso-lines (two columns left) and  $\psi_0(\alpha) = (r_i^1, 0, r_i^2)$  iso-lines (see Eqs. (37) and (38), two columns right) obtained after one revolution of the circular interface on grids  $m_i$ ,  $i = 1, \dots, 4$  (from top to bottom) with the initial condition (black solid line). The results were obtained with  $N_\tau = 0$  (orange double-dashed line),  $N_\tau = 1$  (magenta dashed-dotted line) and  $N_\tau = 32$  (dark blue dashed line) re-initialization steps.

our results and the results presented in [1] is independence of the interface shape from the number of re-initialization steps  $N_\tau \leq 32$ .

To measure the convergence rate of the numerical approximation of the in-

terface  $\Gamma$  towards analytical solution, the first order norm is introduced

$$L_{1,i}^r = \frac{1}{N_i^s} \sum_l^{N_i^s} |\mathbf{r}_{l,i}^{num} - \mathbf{r}_{l,i}^{ext}|, \quad (44)$$

where  $N_i^s$  is the number of points in the interface  $\Gamma$  representation given by the iso-lines of  $\alpha(\psi_0) = 1/2$  or  $\psi_0(\alpha) = 0$ ,  $\mathbf{r}_{l,i}^{num} = |\mathbf{x}_{l,i}^{num} - \mathbf{x}_0|$ ,  $\mathbf{r}_{l,i}^{ext} = |\mathbf{x}_{l,i}^{ext} - \mathbf{x}_0|$ , where  $\mathbf{x}_{l,i}^{num}$  and  $\mathbf{x}_{l,i}^{ext}$  are points obtained from the numerical and the exact approximation of the interface  $\Gamma$  (given by the initial condition) on the grid  $m_i$ . As in the present numerical scheme, we use the first-order discretization method in time. This convergence rate of  $\Gamma$  towards the initial condition is also observed in Tab. 11 for both interface representations. The convergence

$\Gamma$	$\alpha(\psi_0)$			$\psi_0(\alpha)$			
	$N_\tau$	1	16	32	1	16	32
$m_1$		8.3833e-3	8.1417e-3	7.9349e-3	8.5084e-3	8.3689e-3	8.1521e-3
$m_2$		4.4119e-3	4.5067e-3	4.4682e-3	4.3593e-3	4.4516e-3	4.4166e-3
$m_3$		2.1589e-3	2.2262e-3	2.2192e-3	2.1621e-3	2.2296e-3	2.2221e-3
$m_4$		1.0916e-3	1.1243e-3	1.1239e-3	1.0923e-3	1.1247e-3	1.1244e-3

Table 11: The first-order convergence of  $L_{1,i}^r$  norm, computed after one revolution of the circular interface represented by  $\Gamma(\alpha(\psi_0))$  and  $\Gamma(\psi_0(\alpha))$  with  $N_\tau \leq 32$  re-initialization steps.

rate of the reconstructed interface  $\Gamma$  towards the initial condition is related to details in the coupling between equations (32) and (34) and could be improved by introduction of the higher-order discretization schemes. We note that the values of  $L_{1,i}^r$  norm in table 11, remain almost the same in spite of a different number of re-initialization steps  $N_\tau$  used during simulation.

Since the present method uses two representations of the interface  $\alpha(\psi_0)$  and  $\psi_0(\alpha)$ , the area (mass) conservation can be estimated in two different ways. In order to distinguish between these two possibilities, a cumulative error is defined

as

$$E_t = \frac{1}{N_t} \sum_n^{N_t} E_n \quad \text{where} \quad (45)$$

$$E_n = |S_{num}^n - S_{ext}^n| = \int |\alpha_n(\psi_0) - \alpha_n^{ext}(\psi_0^{ext})| dS,$$

and  $\alpha^{ext}$ ,  $\psi_0^{ext}$  are defined by the equations (2) and (36), respectively.  $N_t$  in equation (45) denotes the total number of time steps on the grid  $m_i$  during one revolution of the interface  $\Gamma$ ,  $E_n$  is a difference between the numerical approximation of the surface  $S_{num}^n$  and the exact surface  $S_{ext}^n$  which are calculated on each time level  $n$ . The instantaneous position of the circular interface center  $(x_c, y_c)$  required to compute of  $S_{ext}^n$  is obtained from

$$x_c = \frac{\sum_{i,j} \alpha_{i,j} x_{i,j}}{\sum_{i,j} \alpha_{i,j}}, \quad y_c = \frac{\sum_{i,j} \alpha_{i,j} y_{i,j}}{\sum_{i,j} \alpha_{i,j}}. \quad (46)$$

We found that convergence rates of the area (mass) depend on the region of integration of  $\alpha(\psi_0)$  in Eq. (45). If the region  $r_1 = \{x_i \mid 1 - \alpha(\psi_0) \geq 0.5\}$  or  $r_1 = \{x_i \mid \psi_0(\alpha) \leq 0\}$  is chosen, then the first-order convergence rate of area is obtained, see figures 29(a)-30(a). Similar convergence rates of the Heaviside function were reported in [1] although therein the second-order discretization in time was employed. When the integration is carried out in the region  $r_2 = \{x_i \mid \psi_0(\alpha) \leq 8\epsilon_h\}$  or in the whole computational domain  $\Omega$ , then almost the second-order area convergence rate may be deduced from the results depicted in figure (29)(b). In this latter case, convergence of the interface at each time step  $\Delta t$  with  $N_\tau \leq 32$  (see figure 30(b)) is less evident but may be also observed for example on the grid  $m_4$ . The differences in the magnitude of  $E_t$  errors visible in figures 30(a)(b) may be explained by the more accurate interface representation with the signed distance function, and thus smaller error  $E_n$  during the area (mass) computation in the region  $r_2$ , see Eq. (45).

Here and in the following examples, it becomes clear that  $S_{num}$  calculated in the region  $r_1 = \{x_i \mid 1 - \alpha(\psi_0) \geq 0.5\}$  indicates how the area (mass) varies during topological changes of the interface (stretching, break up, coalescence), whereas  $S_{num}$  calculated in the region  $r_2 = \{x_i \mid \psi_0(\alpha) \leq 8\epsilon_h\}$  allows examina-

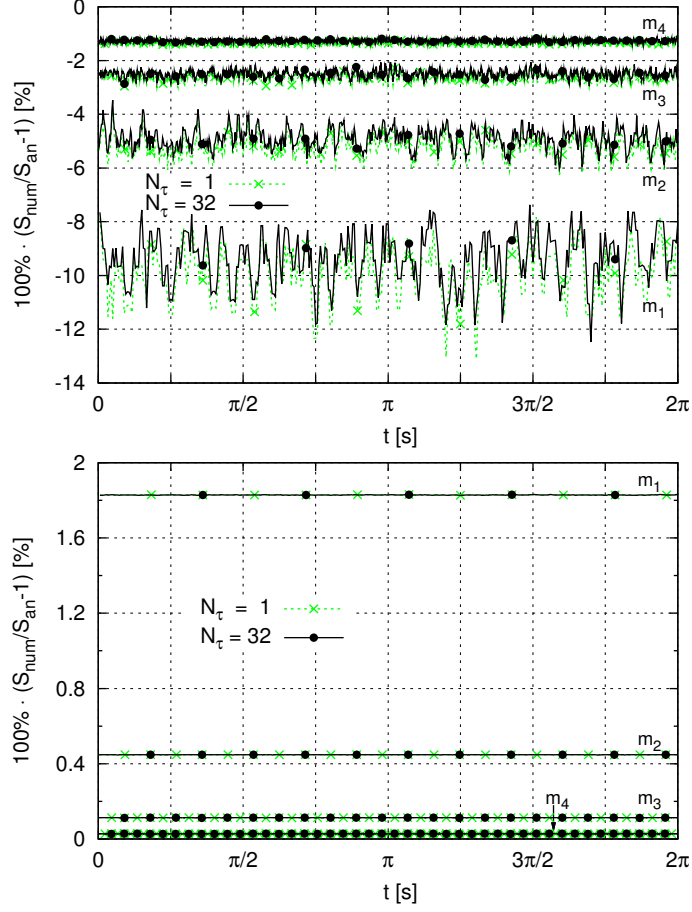


Figure 29: The area conservation calculated in the regions: (a)  $r_1 = \{x_i \mid 1 - \alpha(\psi_0) \geq 0.5\}$ , (b)  $r_2 = \{x_i \mid \psi_0(\alpha) \leq 8\epsilon_h\}$  during one revolution of the circular interface with  $N_\tau = 1$  or  $N_\tau = 32$ , the error is normalized with  $S_{an} = \pi R^2$ .

tion of the total area (mass) conservation. Since the circular interface is rotated as a rigid body in the present case, the errors integrated in both regions  $r_1$  and  $r_2$  remain on constant levels, see Fig. 29.

During rotation of the circular interface without deformations, obtained area convergence rates are almost independent from the number of selected re-initialization steps  $N_\tau$  (compare results with different  $N_\tau$  in Fig. 29 and in Tab. 11). The results presented in figure 30 suggest that in most cases up to

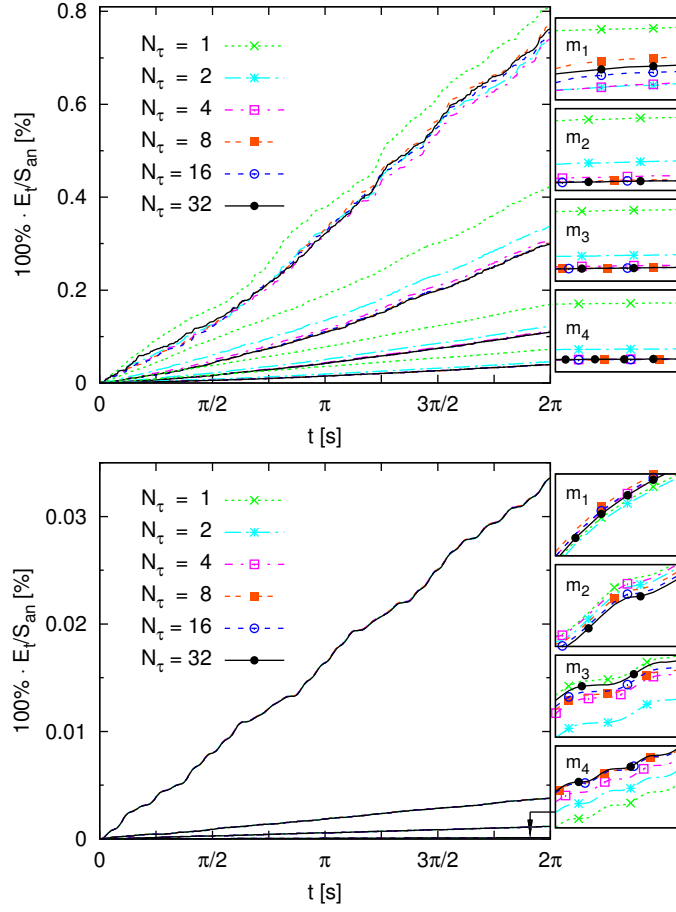


Figure 30: Convergence of the cumulative error  $E_t$  defined by Eq. (45) with the different number of re-initialization steps  $N_\tau \leq 32$ .  $E_t$  is calculated in the regions: (a)  $r_1 = \{x_i \mid 1 - \alpha(\psi_0) \geq 0.5\}$ , (b)  $r_2 = \{x_i \mid \psi_0(\alpha) \leq 8\epsilon_h\}$  and is normalized with  $S_{an} = \pi R^2$ . The boxes on the right, present convergence during last ten time steps  $\Delta t$ , the number and position of symbols is arbitrary.

four re-initialization steps should be sufficient to preserve the shape and area of the interface  $\Gamma$ .

### 6.2.2. Vortex test

To test the new re-initialization method in a more complex velocity field, we use

$$u_1 = -V_0 \sin^2(kx) \sin(2ky), \quad u_2 = V_0 \sin^2(ky) \sin(2kx), \quad (47)$$

where  $k = \pi/L$ ,  $L = 1 \text{ m}$  and  $V_0 = 1 \text{ m/s}$  (similar to the test case in [1]). A circle with the radius  $R = 0.15 \text{ m}$  is initially located at  $(x_0, y_0) = (0.5 \text{ m}, 0.75 \text{ m})$ . The simulation time is  $t = 2 \text{ s}$ , as after time  $T = 1 \text{ s}$  the flow field is reversed so the exact solution should be obtained after the same number of time steps. In order to satisfy the Courant condition  $Cr \approx 0.2$ , the time step size is set to  $\Delta t = \Delta x/8$  to give the total number of time steps per revolution  $N_t = 8T/\Delta x = 8TN_c$ .

The iso-lines of  $\psi_0(\alpha)$  obtained on grids  $m_i$ ,  $i = 1, \dots, 4$  with  $N_\tau = 2$  or  $N_\tau = 16$  are presented in figure 31. For the sake of brevity, iso-lines of  $\alpha(\psi_0)$  are omitted as they are almost identical with iso-lines of  $\psi_0(\alpha)$ . The most important observation in Fig. 31 is that on finer grids, the impact of the number of re-initialization steps  $N_\tau$  on the interface shape becomes negligible. This result shows convergence of the new re-initialization method and is in agreement with studies presented in Fig. 28.

When the present results are compared with the results presented in [1], one notices due to the smaller interface width in our simulations  $\epsilon_h = \sqrt{2}\Delta x/4 < \Delta x/2$  our results are qualitatively similar to the results from [1] on a grid twice as fine. This illustrates the interface width  $\epsilon_h$  is a very important parameter in the present method;  $\epsilon_h$  decides not only whether the interface curvature may be calculated (see Section 5.2) but also governs the topological changes of the interface when the grid resolution is not sufficient to resolve it, see Fig. 31.

After rotation of the interface in the opposite direction with the same number of time steps, the circular interface  $\Gamma$  is reconstructed with the first order accuracy, (see results in figure 32 and in table 12). Similar to the case without interface deformation, the errors in Tab. 12 do not change much with  $N_\tau$ . Convergence towards the initial condition may be observed on the gradually refined grids  $m_i$ ,  $i = 1, \dots, 4$ .

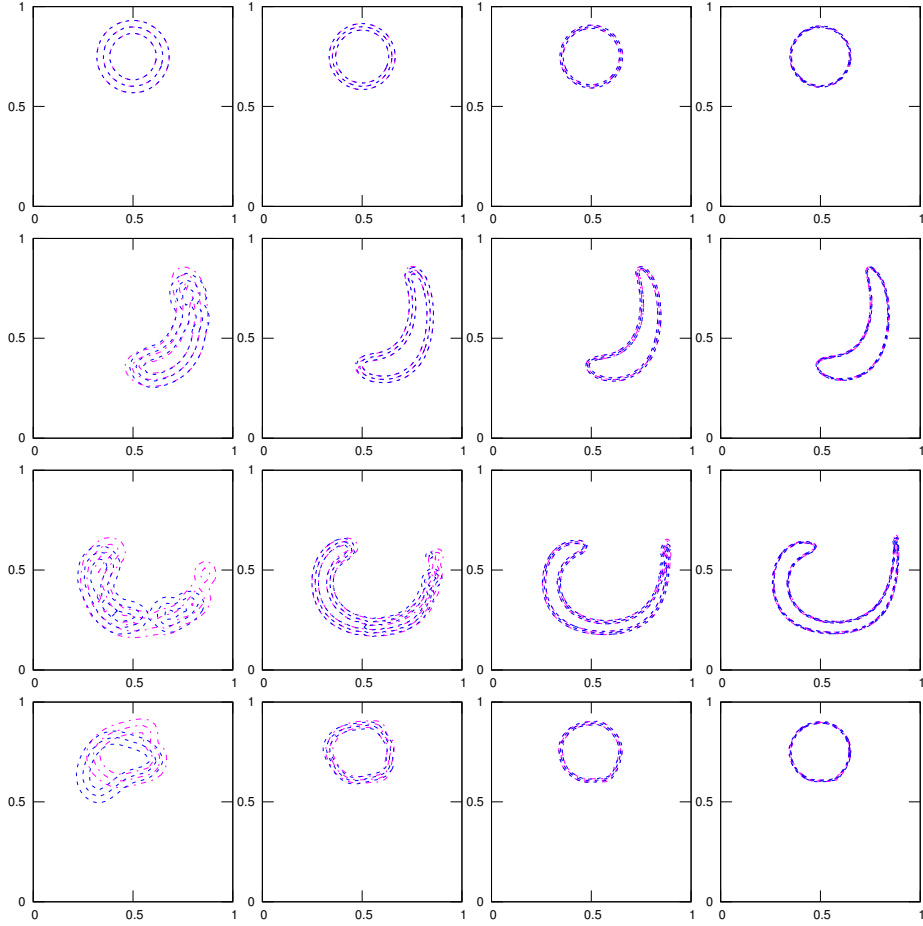


Figure 31: Vortex test on four different grids  $m_i$ ,  $i = 1, \dots, 4$  from left to right at times  $t = 0$ ,  $t = 0.5$ ,  $t = 1.0$ ,  $t = 2.0$  from top to bottom. Figure depicts  $\psi_0(\alpha) = (r_i^1, 0, r_i^2)$  iso-lines (see Eqs. (37) and (38)) with  $N_\tau = 2$  (magenta, dashed-dotted line) and  $N_\tau = 16$  (dark blue, dashed line) re-initialization steps.

The  $L_{1,i}^r$  norm defined in Eq. (44) is not the best measure of interface departure from its original shape as it does not detect oscillations in the reconstructed interface. Closer investigations of the results obtained on the grid  $m_4$  (dark blue dashed line in Fig. 32) reveal that the regularity of the final interface shape at  $t = 2s$  grows with the  $N_\tau$  number. Since re-initialization improves  $\psi_0(\alpha)$ , the errors of  $\mathbf{n}_\Gamma$  remain smaller when  $N_\tau$  is larger and for this reason oscillations

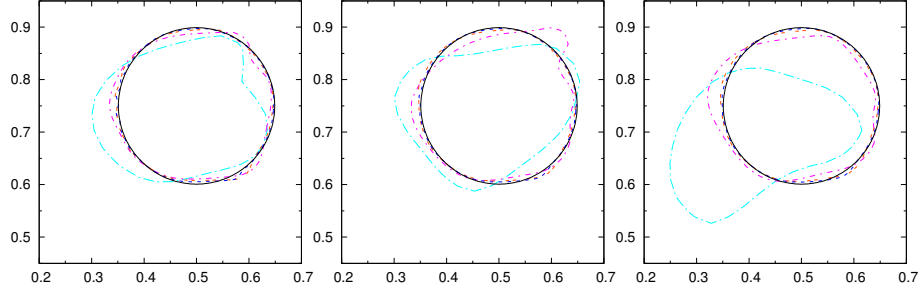


Figure 32: Convergence of  $\psi_0(\alpha) = 0$  iso-lines on grids  $m_i$ ,  $i = 1, \dots, 4$  towards initial condition (black solid line) in the vortex test case with (a)  $N_\tau = 2$ , (b)  $N_\tau = 8$ , (c)  $N_\tau = 16$  re-initialization steps.

$\Gamma$	$\alpha(\psi_0)$			$\psi_0(\alpha)$		
$N_\tau$	2	8	16	2	8	16
$m_1$	2.1424e-1	2.3195e-1	6.8181e-1	2.1434e-1	2.3175e-1	6.8196e-1
$m_2$	7.3558e-3	1.0785e-2	1.1301e-2	7.3921e-3	1.0773e-2	1.1305e-2
$m_3$	3.2984e-3	3.4034e-3	3.5041e-3	3.3082e-3	3.3917e-3	3.4896e-3
$m_4$	1.6404e-3	1.6512e-3	1.6444e-3	1.6467e-3	1.6542e-3	1.6433e-3

Table 12: Convergence of  $L_{1,i}^r$  norm, computed at the end of the vortex test with the  $N_\tau \leq 16$  re-initialization steps. The circular interface is represented by  $\Gamma(\alpha(\psi_0))$  and  $\Gamma(\psi_0(\alpha))$  iso-lines, compare with results in figure (32).

does not appear in the interface shape reconstructed at the end of simulations (compare results on the grid  $m_4$  in figures 32(a) and 32(b)(c)).

In figure 33, the area conservation in the vortex test case is presented. Like in rotation of a rigid body, we also calculate (integrate) errors in two regions  $r_1$  and  $r_2$  in the present case. Since in this case the circular interface is strongly deformed through the vortex velocity field, large variation of the error integrated in the region  $r_1$  is observed, see Fig. 33(a). As the area of the interface  $\Gamma$  increases when it is deformed, the value of the error becomes smaller and then returns to its initial level at the end of the simulation. This result confirms the present re-initialization method is conservative. Similar variation may also be observed in the case of the error obtained in the region  $r_2$ , however the effect is

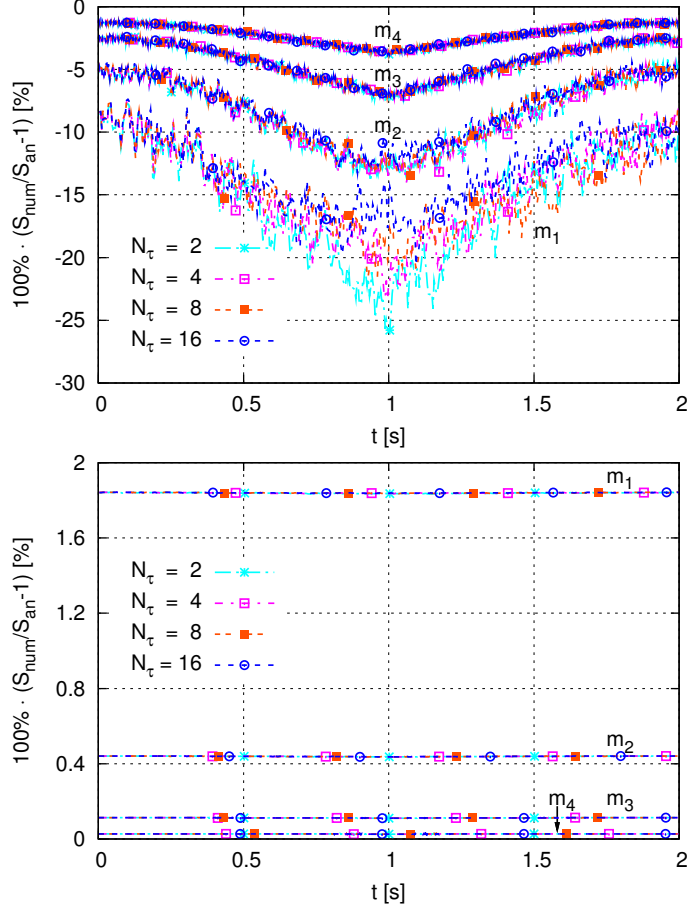


Figure 33: The area conservation calculated in the regions: (a)  $r_1 = \{x_i \mid 1 - \alpha(\psi_0) \geq 0.5\}$ , (b)  $r_2 = \{x_i \mid \psi_0(\alpha) \leq 8\epsilon_h\}$  during vortex test with  $N_\tau \leq 16$ . Error  $S_{num}$  defined in Eq. (45) is normalized with  $S_{an} = \pi R^2$ , the number and position of symbols is arbitrary.

very small, and therefore cannot be observed in Fig. 33(b). The distributions of the errors in Fig. 33(a)(b) confirm that at least the first-order convergence rate of the area (mass) is achieved by the present numerical method. Moreover, we note that the number of re-initialization steps  $N_\tau$  performed on each time step  $\Delta t$  has a small impact on the calculated area when the mesh is sufficiently fine (compare results with different  $N_\tau$  in figures 31 and 33).

To investigate behavior of the new numerical method during longer inte-

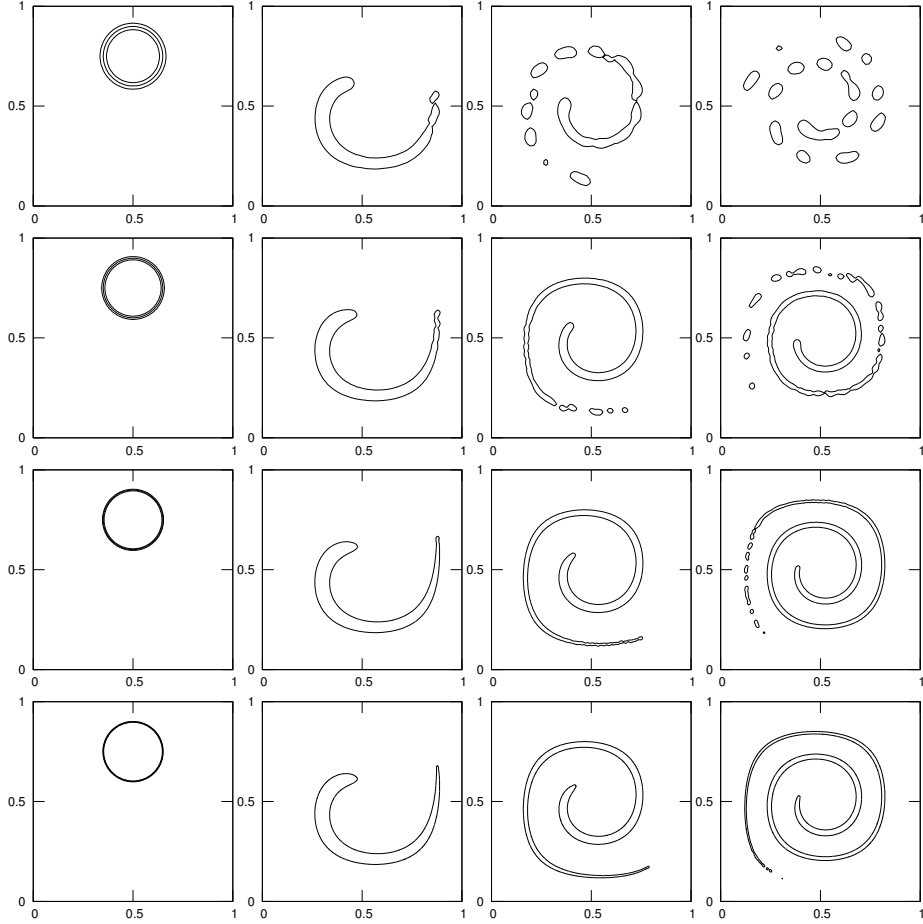


Figure 34:  $\psi_0(\alpha) = 0$  iso-lines, in the vortex test on grids  $m_i$ ,  $i = 2, \dots, 5$  (from top to bottom) after  $T = 0, T = 1, T = 2, T = 3$  revolutions (from left to right), the width of the interface  $\epsilon_h = \sqrt{2}\Delta x/4$ ,  $N_\tau = 4$  on each time step  $\Delta t$ ,  $\Delta\tau = \epsilon_h$ .

gration times (here  $t = 3s$ ), we perform the vortex test without reversing the velocity field after the first revolution. In this test case, we stretch the interface until it is broken into bubbles due to insufficient number of grid points required for its reconstruction. As our advection and re-initialization methods are conservative, and the re-initialization method keeps the prescribed thickness of the interface  $\epsilon_h$  constant, this is the only possible scenario which may occur when the grid resolution is insufficient to resolve the interface  $\Gamma$ . We emphasize

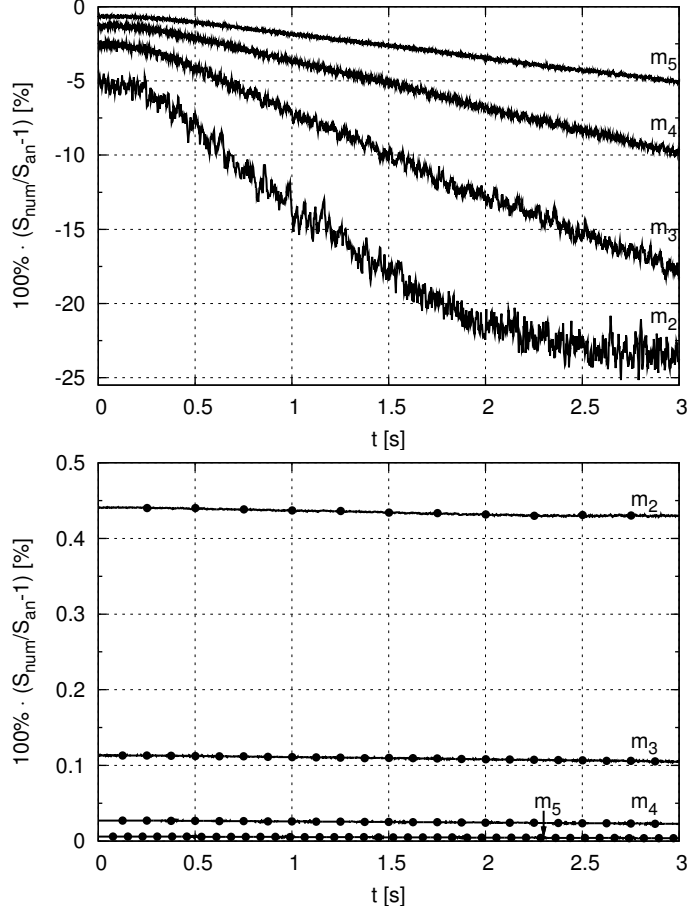


Figure 35: The errors in the area conservation calculated in the regions (a)  $r_1 = \{x_i \mid 1 - \alpha(\psi_0) \geq 0.5\}$ , (b)  $r_2 = \{x_i \mid \psi_0(\alpha) \leq 8\epsilon_h\}$  during vortex test with  $N_\tau = 4$  on each time step  $\Delta t$ . Error  $S_{num}$  defined in Eq. (45) is normalized with  $S_{an} = \pi R^2$ .

that there is no physical mechanism behind the abovementioned break up of the interface. This feature of the present method is direct consequence of its conservative properties.

Using experience gathered in the previous examples, we use  $N_\tau = 4$  re-initialization steps in each single time step  $\Delta t$ ,  $\epsilon_h = \sqrt{2}\Delta x/4$  and  $\Delta\tau = \epsilon_h$ . The results from this study, obtained on four grids  $m_i$  where  $i = 2, \dots, 5$ , at four different time moments  $T$ , are presented in Fig. 34. In order to visualize the

interface thickness on each grid  $m_i$ , at  $T = 0$  three iso-lines of  $\psi_0(\alpha) = (r_i^1, 0, r_i^2)$  (see Eqs. (37) and (38)) are depicted.

We note that the longer the integration time is, the thinner the interface  $\Gamma$  filaments become. However, if the mesh resolution is insufficient to resolve the interface  $\Gamma$ , then the interface break up will occur as this is the only way to preserve the area (mass) correctly.

Errors in the area conservation are depicted in figure 35, where, as in the previous examples,  $S_{num}$  is computed by integration in two regions  $r_1$  and  $r_2$ . The results in Fig. 35 show that the area is conserved in spite of large deformation of the interface  $\Gamma$  on all grids  $m_i$ ,  $i = 2, \dots, 5$ . As discussed previously, the error calculated in the region  $r_1$  permits tracing the impact of the interface deformation on the area (mass) conservation. We note that after break up of the interface into separate bubbles on grid  $m_2$  at the time about  $T = 2.5 s$ , values of  $S_{num}$  integrated in region  $r_1$  cease to drop as the interface deformation is stopped (see Fig. 35(a)). It is expected after large enough integration times  $t \gg 3 s$ , at each grid, the interface will finally disintegrate into droplets that can be transported in the given velocity field.

The total error in the area (mass) conservation, obtained by integration of  $\alpha(\psi_0)$  in the region  $r_2$ , is almost constant on all meshes used in the present study. The loss of total area (mass) is present but negligibly small as shown in figure 35(b).

## 7. Conclusions

In this work, a new re-initialization method of the conservative level-set function was introduced and verified. We have shown that the re-initialization and advection equations of the conservative level-set function  $\alpha(\psi_0)$  are mathematically equivalent to the re-initialization and advection equations of the localized signed distance function  $\psi_0(\alpha)$  (see equations (32) and (34)). It was also proven that the RHS of re-initialization equation (32) is equal to zero when  $|\nabla\psi_0| = 1$ , and  $\alpha(\psi_0) = H(\psi_0)$ . These two solutions to the re-initialization equation

(32) permit computing the interface curvature, and controlling its thickness  $\epsilon_h < \Delta x/2$  which assures the improvement of the spatial resolution of the new method, see discussion in Sec. 5.2 and the results in Sec. 6.

In the present re-initialization procedure, the conservative level-set function  $\alpha(\psi_0)$  remains continuous and bounded inside the support of  $\delta(\alpha)/\epsilon_h = \alpha(1-\alpha)/\epsilon_h$  function. For this reason, we do not need to use the fast marching method, required in other re-initialization techniques reported in the literature, in order to extend the signed distance function  $\psi_0(\alpha)$  away from the interface  $\Gamma$ . The continuity of the solution assured by the new re-initialization method avoids artificial interface deformations, which are eventually introduced by the flux limiters typically used to bound counteracting compressive and diffusive fluxes on the RHS of Eq. (1). In the light of the other results presented in the literature, the new re-initialization method shows fast convergence and in the 1D cases, reconstructs exact behavior of the analytical solution to the partial differential equation (1), see Fig. 4.

Discretization of the first and second-order spatial derivatives of  $\alpha(\psi_0)$ , which is consistent with the discretization of the re-initialization equation and the theory of distributions, achieves the second-order convergence rate of the interface curvature  $\kappa$ , see Eq. (35). Such level of accuracy is obtained in the second-order accurate finite volume solver without geometrical reconstruction of the interface or an introduction of the higher-order essentially non-oscillatory interpolation schemes in the discretization procedure.

The advection tests performed in Section 6.2 show the new method conserves the total area (mass) with almost second order accuracy, and the shape of the advected interface is independent from the number of the re-initialization steps if the spatial and temporal resolutions are sufficient.

The new re-initialization method presented herein may be considered a backbone of the conservative level-set method, a potentially good replacement for the compressive interface capturing schemes commonly used in the fast multiphase flow solvers. Its implementation is simple and its strengths include accurate reconstruction of the interface curvature and conservation of the area (mass)

without smearing the interface.

## Acknowledgments

The work was funded by the German Research Foundation (DFG) in the framework of the project "Modeling of turbulence-interface interactions in two-fluid systems" WA: 3098/2-1, AOBJ: 595642.

## Appendix A. Limits of the mapping function

In this appendix, the limits of the level-set function  $\alpha(\psi_0(\mathbf{x}, t))$  and the mapping function  $\psi_1(\alpha, \gamma)$  given by Eq. (2) and Eq. (8) are calculated. Since in this section we consider analytical properties of  $\psi_1(\alpha, \gamma)$  next  $\epsilon = 0$  in equation (8). We assume that the number of grid nodes  $N_c \rightarrow \infty$  and  $0 < \gamma \ll \Delta x$  is a small constant. The analytical solution given by Eq. (2) may be rewritten as

$$\alpha = \frac{1}{2} \left[ 1 + \tanh \left( \frac{\psi_0}{2\epsilon_h} \right) \right] = \frac{1}{1 + \exp(-2N_c\psi_0)} \quad (\text{A.1})$$

where  $N_c = 1/\Delta x$  and  $\psi_0$  is the signed distance function given by Eq. (3). Additionally, we rearrange Eq. (14) into

$$\psi_1 = \frac{\exp(N_c\psi_0\gamma)}{\exp(N_c\psi_0\gamma) + \exp(-N_c\psi_0\gamma)} = \frac{1}{1 + \exp(-2N_c\psi_0\gamma)}. \quad (\text{A.2})$$

First, we note that if  $\gamma \rightarrow 0$  in Eq. (A.2),  $\psi_1 \rightarrow 1/2$  as it was observed in [2]. Let us now consider three limits of Eq. (A.1) and Eq. (A.2) when  $N_c\gamma \rightarrow \infty$  and  $0 < \gamma \ll \Delta x$ :

1. when  $\psi_0 < 0$  :  $\psi_1 \rightarrow 0, \alpha \rightarrow 0,$
2. when  $\psi_0 = 0$  :  $\psi_1 = 1/2, \alpha = 1/2,$
3. when  $\psi_0 > 0$  :  $\psi_1 \rightarrow 1, \alpha \rightarrow 1$

Hence, when the number of grid points  $N_c \rightarrow \infty$  and  $\gamma = \text{const}$  functions  $\psi_1$  and  $\alpha$  become the Heaviside function  $H(\psi_0)$ . The phase indicator function  $H(\psi_0)$  is typically discretized in the volume of fluid (VOF) methods [8].

## Appendix B. Discretization of the re-initialization equation

In this appendix, the discretization of Eq. (1) or equivalent Eqs. (32) and (33) in the framework of the second order accurate finite volume method is presented. Since all terms on the RHS of Eq. (33) are in the form of the mass forces, after its integration in the control volume  $V_P$  one would obtain

$$\begin{aligned} \left. \frac{\partial \alpha}{\partial \tau} \right|_P &= [\mathbf{n}_\Gamma \cdot \nabla \delta(\alpha) (|\nabla \phi| - 1)]|_P \\ &+ [\mathbf{n}_\Gamma \cdot \nabla (|\nabla \phi| - 1) \delta(\alpha)]|_P \\ &- [\kappa (|\nabla \phi| - 1) \delta(\alpha)]|_P, \end{aligned} \quad (\text{B.1})$$

where  $\mathbf{n}_\Gamma = \nabla \phi / |\nabla \phi|$  and  $\phi$  is equal to  $\alpha(\mathbf{x}, t)$  or is one of the mapping functions  $\psi_1(\alpha, \gamma)$ ,  $\psi_0(\alpha)$ . Eq. (B.1) is the discretization to the non-conservative form of Eq. (1), all terms with sub-script  $P$  can be obtained from the values stored in the centers of the control volumes.

In the present work, we use the conservative discretization to Eq. (1) or equivalent Eq. (32). After integration of Eq. (32) in the control volume  $V_P$ , employment of the Gauss theorem and mid-point rule at the centers of faces  $f$  and in the centers of control volume  $P$  one obtains

$$\left. \frac{\partial \alpha}{\partial \tau} \right|_P = \frac{1}{V_P} \sum_{f=1}^{n_b} [\delta(\alpha) (|\nabla \phi| - 1) \mathbf{n}_\Gamma \cdot \mathbf{n}]_f S_f, \quad (\text{B.2})$$

where  $n_b$  is the number of neighbors of the control volume  $P$ ,  $[\mathbf{n}_\Gamma \cdot \mathbf{n}]_f$  is dot product of the normal  $\mathbf{n}_\Gamma = \nabla \phi / |\nabla \phi|$  interpolated to the face  $f$  and normal  $\mathbf{n}_f$  at the face  $f$ ,  $\delta(\alpha)$  is defined by Eq. (25);  $|\nabla \phi|$  is computed using the second-order central-difference approximation to the  $\phi$  gradient components, at face  $f = e$  this approximation reads

$$\begin{aligned} \left. \frac{\partial \phi}{\partial x_1} \right|_e &\approx \frac{(\phi_E - \phi_P)}{\Delta x}, \\ \left. \frac{\partial \phi}{\partial x_2} \right|_e &\approx \frac{(\phi_N + \phi_{NE} - \phi_S - \phi_{SE})}{4\Delta y}, \\ \left. \frac{\partial \phi}{\partial x_3} \right|_e &\approx \frac{(\phi_T + \phi_{TE} - \phi_B - \phi_{BE})}{4\Delta z}, \end{aligned} \quad (\text{B.3})$$

where subscript  $E, N, T, \dots$  represent the centers of the neighbor control volumes. The interpolation to the faces  $f$  of the control volume  $P$  is performed

using second-order accurate linear interpolation scheme, which on uniform grids simplifies to  $\phi_f = 1/2(\phi_F + \phi_P)$ , see [26, 27]. Dependent on the test case,  $\phi$  in Eq. (B.3) is calculated using  $\alpha(\mathbf{x}, t)$  or  $\psi$  obtained from the mapping functions given by Eq. (3) or Eq. (8) with different  $\gamma$  values.

## References

- [1] E. Olsson, G. Kreiss, A conservative level-set method for two phase flow, *J. Comput. Phys.* 210 (2005) 225–246.
- [2] R. Shukla, C. Pantano, J. Freund, An interface capturing method for the simulation of mutli-phase compressible flows, *J. Compt. Phys.* 229 (2010) 7411–7439.
- [3] K. So, X. Hu, N. Adams, Anti-diffusion method for interface steepening in two-phase incompressible flows, *J. Compt. Phys.* 230 (2011) 5155–5177.
- [4] A. Tiwari, J. Freund, C. Pantano, A diffuse interface model with immiscibility preservation, *J. Compt. Phys.* 252 (2013) 290–309.
- [5] N. Balczar, L. Jofre, O. Lehmkuhl, J. Castro, J. Rigola, A finite-volume/level-set method for simulating two-phase flows on unstructured grids, *International Journal of Multiphase Flow* 64 (0) (2014) 55 – 72. doi:<http://dx.doi.org/10.1016/j.ijmultiphaseflow.2014.04.008>.
- [6] K. Glasner, Nonlinear preconditioning for diffuse interfaces, *Journal of Computational Physics* 174 (2) (2001) 695 – 711. doi:<http://dx.doi.org/10.1006/jcph.2001.6933>.
- [7] Y. Sun, C. Beckermann, Sharp interface tracking using the phase-field equation, *Journal of Computational Physics* 220 (2) (2007) 626 – 653. doi:<http://dx.doi.org/10.1016/j.jcp.2006.05.025>.
- [8] G. Tryggvason, R. Scardovelli, S. Zaleski, *Direct Numerical Simulations of Gas-Liquid Multiphase Flows*, Cambridge University Press, 2011.

- [9] S. Osher, J. A. Sethian, Fronts propagating with curvature-dependent speed: Algorithms based on Hamilton-Jacobi formulations, *Journal of Computational Physics* 79 (1) (1988) 12 – 49. doi:[http://dx.doi.org/10.1016/0021-9991\(88\)90002-2](http://dx.doi.org/10.1016/0021-9991(88)90002-2).
- [10] M. Sussman, P. Smereka, S. J. Osher, A level set approach for computing solutions to incompressible two-phase flows, *J. Comput. Phys* 114 (1994) 146–159.
- [11] M. Sussman, E. Fatemi, P. Smereka, S. Osher, An improved level set method for incompressible two-phase flows, *Computers and Fluids* 27 (56) (1998) 663 – 680. doi:[http://dx.doi.org/10.1016/S0045-7930\(97\)00053-4](http://dx.doi.org/10.1016/S0045-7930(97)00053-4).
- [12] S. Osher, R. Fedkiw, *Level Set Methods and Dynamic Implicit Surfaces*, Springer Verlag, INC. New-York, 2003.
- [13] D. Hartmann, M. Meinke, W. Schröder, The constrained reinitialization equation for level set methods, *Journal of Computational Physics* 229 (5) (2010) 1514 – 1535. doi:<http://dx.doi.org/10.1016/j.jcp.2009.10.042>.
- [14] G. D. Rocca, G. Blanquart, Level set reinitialization at a contact line, *Journal of Computational Physics* 265 (0) (2014) 34 – 49. doi:<http://dx.doi.org/10.1016/j.jcp.2014.01.040>.
- [15] E. Olsson, G. Kreiss, S. Zahedi, A conservative level set method for two phase flow II, *Journal of Computational Physics* 225 (1) (2007) 785 – 807. doi:<http://dx.doi.org/10.1016/j.jcp.2006.12.027>.
- [16] J. O. McCaslin, O. Desjardins, A localized re-initialization equation for the conservative level set method, *Journal of Computational Physics* 262 (0) (2014) 408 – 426. doi:<http://dx.doi.org/10.1016/j.jcp.2014.01.017>.
- [17] S. Gottlieb, S. C.-W., Total variation diminishing Runge-Kutta schemes, *Mathematics of Computation* 67 (1998) 73–85.

- [18] I. Bronstein, K. Semendajew, G. Musiol, H. Mülig, Tachenbuch der Mathematik, Harri Deutsch, 2012.
- [19] O. Ubbink, R. Issa, Method for capturing sharp fluid interfaces on arbitrary meshes, *J. Comput. Phys.* 153 (1999) 26–50.
- [20] T. Waławczyk, T. Koronowicz, Modelling of the free surface flows with high-resolution schemes, *Chemical and Process Engineering* 27 (2006) 783–802.
- [21] T. Waławczyk, T. Koronowicz, Comparison of CICSAM and HRIC high resolution schemes for interface capturing, *J. Theoretical and Applied Mechanics* 46 (2008) 325–345.
- [22] T. Waławczyk, T. Koronowicz, Remarks on prediction of wave drag using VOF method with interface capturing approach, *Archives of Civil and Mechanical Engineering* 8 (1) (2008) 5 – 14. doi:[http://dx.doi.org/10.1016/S1644-9665\(12\)60262-3](http://dx.doi.org/10.1016/S1644-9665(12)60262-3).
- [23] M. Waławczyk, M. Oberlack, Closure proposals for the tracking of turbulence-agitated gas-liquid interfaces in stratified flows, *Int. J. Multiphase Flow* 37 (2011) 967–976.
- [24] T. Waławczyk, M. Waławczyk, S. V. Kraheberger, Modelling of turbulence-interface interactions in stratified two-phase flows, *Journal of Physics: Conference Series* 530.
- [25] M. Waławczyk, T. Waławczyk, A priori study for the modelling of velocity-interface correlations in the stratified airwater flows, *International Journal of Heat and Fluid Flow* 52 (0) (2015) 40 – 49. doi:<http://dx.doi.org/10.1016/j.ijheatfluidflow.2014.11.004>.
- [26] J. H. Ferziger, M. Perić, *Computational Methods for Fluid Dynamics*, Springer Verlag, Berlin Heidelberg New York, 2002.

- [27] M. Schäfer, Computational Engineering, Introduction to Numerical Methods, Springer-Verlag Berlin Heidelberg New York, 2006.
- [28] L. Xue, Entwicklung eines effizienten parallelen lösungsalgorithmus zur dreidimensionalen simulation komplexer turbulenter strömungen, Ph.D. thesis, Doktorarbeit, Technische Universität Berlin (1998).